Innovative tools for offshore wind and DC grids

Deliverable 1.5 – Work Package 1
Report on the toolboxes and experimental validation of design, and models of DC transformer, EMS and SCADA.

Dissemination level	Other
Website	http://innodc.org/
Grant Agreement number	765585
Due delivery	Month 36: 31 August 2020
Project dates	01/09/2017 – 31/08/2021

Authors	**Names**
ESR1	Peng Yang
ESR4	Davide Pinzan
ESR5	Daniel Westerman Spier
ESR12	Stephen Hardy
ESR14	Motaz Ayiad
Supervisor (KU Leuven)	Hakan Ergun
Supervisor (UPC) WP1 leader	Eduardo Prieto-Araujo

Summary

This document contains a description of the InnoDC project Deliverable 1.5. It develops toolboxes to model SiC MOSFETs for power electronics converters and to design the controller for DC transformers.

Contents

1 Introduction **4**
1.1 DC transformer switches modelling 4
1.2 Controller design of DC transformers 5

2 Toolbox to model SiC MOSFET switches for DC transformer **6**
2.1 Model Description 6
2.1.1 I_{DS} model 7
2.1.2 Diode model 7
2.1.3 Capacitance models 8
2.2 Step-by-step modelling approach 8
2.2.1 Modelling approach of I_{DS} at 25 °C 8
2.2.2 Modelling approach of I_{DS} with temperature dependency 13
2.2.3 Modelling approach of diode 13
2.2.4 Modelling approach of parasitic capacitors 15
2.3 Model verification 18
2.4 Toolbox to model SiC MOSFETs 19

3 Toolbox to design voltage controller of DC transformers **22**
3.1 Transfer function of DC transformer 22
3.2 Controller design 23
3.3 Validation 24
3.4 Toolbox to design voltage controller of DC transformers 25

4 Power SCADA/EMS Systems **26**
4.1 SCADA Components and Structure 27
4.1.1 Operator Room station 27
4.1.2 Communication Infrastructure 28
4.1.3 Master and Remote Terminal Units 32
4.2 SCADA/EMS Functions, Managements and Toolboxes 33
4.2.1 Operations Management 33
4.2.2 Power Application Software (PAS) 34

5 The Unified Weighted Least Squares (WLS) State estimator toolbox **36**
5.1 Weighted Least Squares (WLS) algorithm 36
5.1.1 AC Power flow calculations 38
5.1.2 DC Power flow calculations 39
5.1.3 Converter Power coupling 40
5.1.4 Converter voltage coupling 41

5.2 The Unified WLS for VSC HVDC/AC modifications 42
5.3 State estimation simulations 44
5.3.1 Four(4)-AC/four(4)-DC/four(4)-AC network 46

6 Conclusions **51**

1 Introduction

1.1 DC transformer switches modelling

Semiconductor switches are the key component to build power electronic converters such as MMC and DC transformers. Silicon Carbide (SiC) MOSFETs have become very attractive for high efficiency and high power density applications due to their superior properties. Compared to Si IGBTs, SiC MOSFETs have the advantages of low on-resistance, fast switching speed, low switching losses and high junction temperature capability [1]. However, high switching speed of SiC devices brings to more serious electromagnetic interface (EMI) issues due to the higher dv/dt and di/dt during the switching transients [2]. Moreover, the efficiency and power density of the converters highly depend on the switching losses during the switching transients. Experimental approaches can be used to mitigate EMI issues and optimize the efficiency and power density by multiple rounds of prototype testing, which are both time and money consuming. An alternative approach is the simulation-based design of power electronic converters. To accurately simulate the EMI and switching losses, an accurate transient model of SiC MOSFETs is required to predict the waveforms of the switching transients [3].

Although many manufacturers have provided simulation models for their discrete SiC MOSFETs, there are very few commercial models for SiC MOSFET power modules. The converter designers often need to build the model for the power modules by themselves. However, most converter designers are not semiconductor experts. A simple and detailed modelling approach that can be used for various SiC MOSFET power modules is required to help these designers.

There have been various models presented in the literature [4]. An accurate SiC MOSFET model is built in [2] by measuring the I_{DS}-V_{DS} characteristics of the high-voltage and high-current region and the on-state capacitance characteristics. However, additional measurement equipment and test circuits are required for this model, which might not be available for converter designers. From this perspective, a datasheet-based modelling approach without additional experimental measurements is preferred because it can be adopted by all designers. A datasheet-based SiC MOSFET model is proposed in [5] with wide temperature range. Another accurate subcircuit model of SiC half-bridge modules is proposed in [3] for switching-loss optimization based on datasheet information. However, both models used segmented capacitance models which might cause a convergence problem [6]. To solve the convergence problem, a non-segmented model is proposed in [7].

SiC MOSFET models usually contain complicated nonlinear equations and multiple parameters to accurately model the current and capacitance characteristics. Although the same model can be used for different power modules, the parameters in the model are distinct. Therefore, the model parameters should be extracted based on the datasheet of specific power modules. Although there are various models in the literature, the parameter extraction procedure of these models is either too complicated or not well-established, which hinders the application of the models for converter designers. Therefore, a step-by-step parameter extraction procedure is required.

In this report, a toolbox to model SiC MOSFET half-bridge power modules is proposed. The proposed step-by-step modelling approach considers temperature characteristics. The drain-to-source current, anti-parallel diode and parasitic capacitors are accurately modelled based on datasheet. The temperature dependency is considered. A step-by-step parameter extraction approach of each component is clearly introduced. A SPICE model for a commercial power module is built based on the proposed modelling approach. The established model is verified by comparing experiment and PSpice simulation results of the same double pulse tester (DPT). This modelling approach can be easily applied to model other SiC MOSFET power modules so that it can help converter designers develop their own model quickly and accurately.

1.2 Controller design of DC transformers

The DC transformer (i.e. DC/DC converter) for Direct Current (DC) grids is still a developing technology. The motivation of researching DC transformers for DC grids is the rapid growth of High Voltage DC (HVDC) transmission lines in Europe, China and all around the world. In the future, these point-to-point HVDC links can be interconnected to build a DC grid. However, nowadays the HVDC links are designed without standardization. The HVDC links are designed at different voltage levels, different ground configurations, and different valves (VSC or LCC). Therefore, to interconnect these HVDC links to form a future DC grids, DC transformers are necessary.

In Deliverable 1.1, different topologies of DC transformers for DC grids have been discussed. In Deliverable 1.2, The modulation, control strategy, and protections of the DAB-based DC transformer is presented. In this report, a toolbox to design the voltage controller of the DAB-based DC transformer is presented and validated.

((a)) ((b))

Figure 1: A 1200-V 120-A SiC MOSFET Half-Bridge Power Module CAS120M12BM2: (a) Package, (b) Schematic,

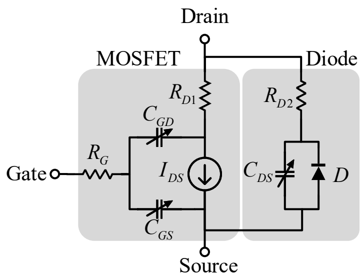

Figure 2: Subcircuit model of a pair of SiC MOSFET and anti-parallel diode in the power module.

2 Toolbox to model SiC MOSFET switches for DC transformer

2.1 Model Description

A 1200V 120A SiC half-bridge module CAS120M12BM2 [8] from Wolfspeed is used to explain the proposed modelling approach. The same approach can be used for other SiC MOSFETs. The power module is shown in Fig 1(a). As shown in Fig. 1(b), the half-bridge module is packaged with two pairs of SiC MOSFETs and anti-parallel SiC Schottky diodes. Fig. 2 shows the subcircuit model of a pair of SiC MOSFET and anti-parallel diode in the module. The model consists of three major parts: drain-to-source current I_{DS} model, diode model and capacitance models. These three parts are modelled as follows.

2.1.1 I_{DS} model

In Fig. 2, a voltage-controlled current source I_{DS} and a series resistor R_{D1} are used to model the drain-to-source current of the SiC MOSFET. The model is based on the standard MOSFET level 1 SPICE model [9]:

if $V_{DS} < 0$ or $V_{GS} < V_{GS(th)}$,

$$I_{DS} = 0 \tag{1}$$

if $0 < V_{DS} < V_{GS} - V_{GS(th)}$,

$$I_{DS} = K_p \left(V_{GS} - V_{GS(th)} - \frac{V_{ch}}{2} \right) V_{ch} \left(1 + \lambda V_{ch}\right) \tag{2}$$

if $V_{DS} > V_{GS} - V_{GS(th)}$,

$$I_{DS} = K_p \frac{\left(V_{GS} - V_{GS(th)}\right)^2}{2} \left(1 + \lambda V_{ch}\right) \tag{3}$$

$$K_p = K_{p1} + K_{p2} \left(V_{GS} - 10\right) \tag{4}$$

$$V_{ch} = V_{DS} - R_{D1} I_{DS} \tag{5}$$

where V_{GS} and V_{DS} are respectively the gate-to-source and the drain-to-source voltages; V_{ch} is the channel voltage applied to the voltage-controlled current source I_{DS}; $V_{GS(th)}$ is the gate threshold voltage; λ is the coefficient of short-channel effect; K_p is the transconductance coefficient, which is modelled as a linear function of V_{GS} with two parameters K_{p1} and K_{p2} in (4). In the I_{DS} model, K_{p1}, K_{p2}, $V_{GS(th)}$, R_{D1} and λ are the parameters that need to be extracted according to the datasheet. Furthermore, to consider the temperature characteristics, K_{p1}, K_{p2}, $V_{GS(th)}$ and R_{D1} are modelled as linear or quadratic functions of temperature: $K_{p1}(T)$, $K_{p2}(T)$, $V_{GS(th)}(T)$ and R_{D1}(T), based on the curve fitting results. The detailed modelling approach will be described in Section 2.2.

2.1.2 Diode model

In Fig. 2, a voltage-controlled current source I_D and a series resistor R_{D2} are used to model the current behavior of the anti-parallel diode. The model can be described in the following equations:

$$I_D = I_S \left(\exp\left(\frac{qV_D}{kT} \right) - 1 \right) \tag{6}$$

$$V_D = V_{SD} - R_{D2} I_D \tag{7}$$

where V_{SD} is the source-to-drain voltage; V_D is the diode voltage applied to the voltage-controlled current source I_D; I_S is the reverse saturation current; $q = 1.602 \times 10^{-19}$ C is the elementary charge; $k = 1.3806488 \times 10^{-23}$ J/K is the Boltzmann's constant; T is the Kelvin temperature.

2.1.3 Capacitance models

In Fig. 2, three capacitors, C_{GS}, C_{GD} and C_{DS}, are used to model the parasitic capacitors of the SiC MOSFET. C_{GS} is modelled as a constant capacitor. C_{DS} and C_{GD} are modelled as nonlinear capacitors as shown in (8) [3] and (9) [10].

$$C_{DS} = C_{DS0} \left(\frac{V_{bi}}{V_{DS} + V_{bi}} \right)^{M_{CDS}} \tag{8}$$

$$C_{GD} = \frac{C_{GD0}}{\left(1 + V_{DG} \left(1 + k_1 \frac{1 + \tanh\left(k_2 (V_{DG} - V_T)\right)}{2} \right) \right)^{M_{CGD}}} \tag{9}$$

where V_{DG} is the drain-to-gate voltage; C_{DS0}, V_{bi}, M_{CDS} are the parameters for C_{DS}; C_{GD0},M_{CGD}, k_1, k_2 and V_T are the parameters for C_{GD}.

2.2 Step-by-step modelling approach

2.2.1 Modelling approach of I_{DS} at 25 °C

Firstly, the modelling approach of I_{DS} at 25 °C is described. The same modelling approach can be used for I_{DS} model at different temperatures. The parameters K_{p1}, K_{p2}, $V_{GS(th)}$, R_{D1} and λ need to be extracted based on the I_{DS}–V_{GS} transfer characteristics and I_{DS}–V_{DS} output characteristics at 25 °C from the datasheet as shown in Fig. 3. The software GetData Graph Digitizer is used to convert the graphs of I_{DS} characteristics in the datasheet into digital data. MATLAB curve fitting toolbox is used to do the curve fitting to extract parameters.

1) Coefficient of short-channel effect λ

Due to the short-channel effect, the channel length modulation occurs in SiC MOSFETs, which makes the positive current slope in the saturation region [11]. The short channel effect can be observed in Fig. 3(a) in the saturation region when $V_{GS} = 10\,\text{V}$. In the saturation region, V_{ch} is the dominant factor

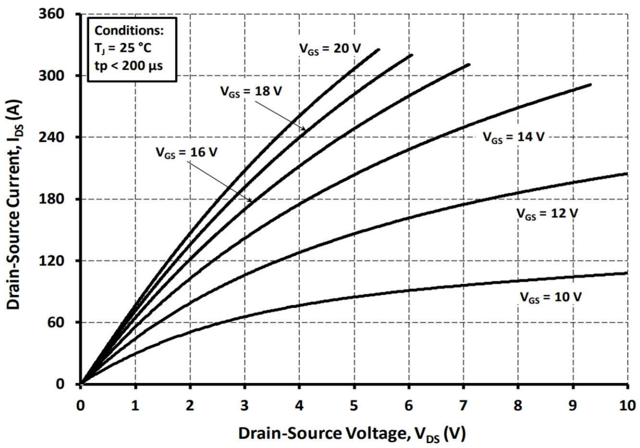

((a)) I_{DS}–V_{DS} output characteristics at 25 °C.

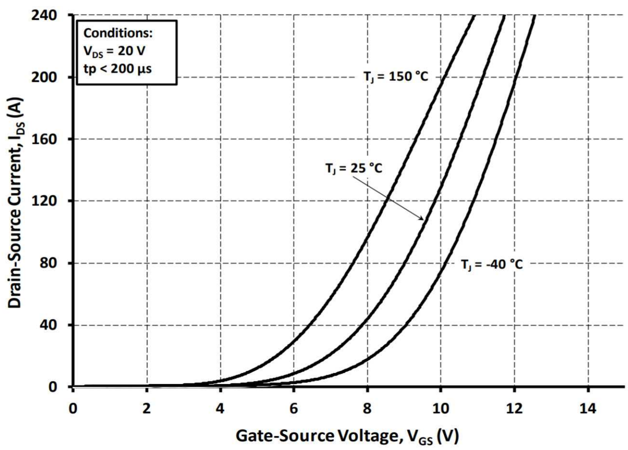

((b)) I_{DS}–V_{GS} transfer characteristics.

Figure 3: I_{DS} characteristics of CAS120M12BM2 in the datasheet.

of V_{DS} due to the high channel resistance when the channel is pinched off. The voltage drop on R_{D1} can be ignored. It can be assumed that $V_{ch} \approx V_{DS}$. Therefore, V_{ch} in (3) can be replaced with V_{DS}. (3) can be simplified as:

$$I_{DS} = A(1 + \lambda V_{DS}) \tag{10}$$

where $A = K_p \frac{\left(V_{GS} - V_{GS(th)}\right)^2}{2}$ is a constant value when $V_{GS} = 10\,\mathrm{V}$. λ can be extracted by curve fitting to fit (10) to the saturation region of I_{DS}–V_{DS} curve when $V_{GS} = 10\,\mathrm{V}$ in Fig. 3(a).

2) Gate threshold voltage $V_{GS(th)}$

The gate threshold voltage is defined as the gate-to-source voltage when the MOSFET starts to conduct a certain small amount of current. However,

Table 1: Extracted K_p with different V_{GS}.

V_{GS}	10 V	12 V
K_p	4.886	5.450

different MOSFETs and manufacturers might have different criteria of this current magnitude from 1 mA up to 50 mA. Therefore, it is better to extract the $V_{GS(th)}$ for the model, although it is already provided in the datasheet [3]. In the datasheet, the transfer characteristics, i.e. the I_{DS}–V_{GS} curve, are usually measured with a high drain-to-source voltage bias so that I_{DS} is saturated. For example, in the datasheet of CAS120M12BM2, $V_{DS} = 20\,\mathrm{V}$ is used to measure the transfer characteristics as shown in Fig. 3(b). In the saturation region, $V_{ch} \approx V_{DS}$ can be assumed, since V_{ch} is the dominant factor of V_{DS} . Therefore, V_{ch} in (3) can be replaced with $V_{DS} = 20\,\mathrm{V}$. (3) can be simplified as:

$$I_{DS} = B\frac{\left(V_{GS} - V_{GS(th)}\right)^2}{2} \tag{11}$$

where $B = K_p(1 + \lambda V_{DS})$ is a constant value when $V_{DS} = 20\,\mathrm{V}$. $V_{GS(th)}$ can be extracted by curve fitting to fit (3) to the I_{DS}–V_{GS} curve in Fig. 3(b).

3) Transconductance coefficient K_p

Two sets of I_{DS}–V_{DS} curves are required since the transconductance coefficient is modelled with two parameters K_{p1} and K_{p2} in (4). The I_{DS}–V_{DS} curves when $V_{GS} = 10\,\mathrm{V}$ and $12\,\mathrm{V}$ are chosen due to the high channel resistance at low gate-to-source voltage. Therefore, the voltage drop on R_{D1} can be ignored and $V_{ch} \approx V_{DS}$ can be assumed. In this case, V_{ch} in (2) can be replaced with V_{DS}. (2) can be rewritten as:

$$I_{DS} = K_p\left(V_{GS} - V_{GS(th)} - \frac{V_{DS}}{2}\right)V_{DS}\left(1 + \lambda V_{DS}\right) \tag{12}$$

K_p can be extracted by curve fitting to fit (12) to the linear region of I_{DS}–V_{DS} curves when $V_{GS} = 10\,\mathrm{V}$ and $12\,\mathrm{V}$ in Fig. 3(a) respectively. Two different values of K_p can be extracted with $V_{GS} = 10\,\mathrm{V}$ and $12\,\mathrm{V}$ respectively as shown in Table 1. Afterwards, (4) can be used to fit Table 1 to extract K_{p1} and K_{p2}.

4) Series resistance R_{D1}

In the model shown in Fig. 2, the on-state resistance $R_{DS(on)}$ consists of the channel resistance R_{ch} of the current source I_{DS} and the series resistance R_{D1}. $R_{DS(on)}$ is provided in the datasheet at specific conditions. For example, in the datasheet of CAS120M12BM2, $R_{DS(on)} = 13\,\mathrm{m\Omega}$ when $V_{GS} = 20\,\mathrm{V}$ and

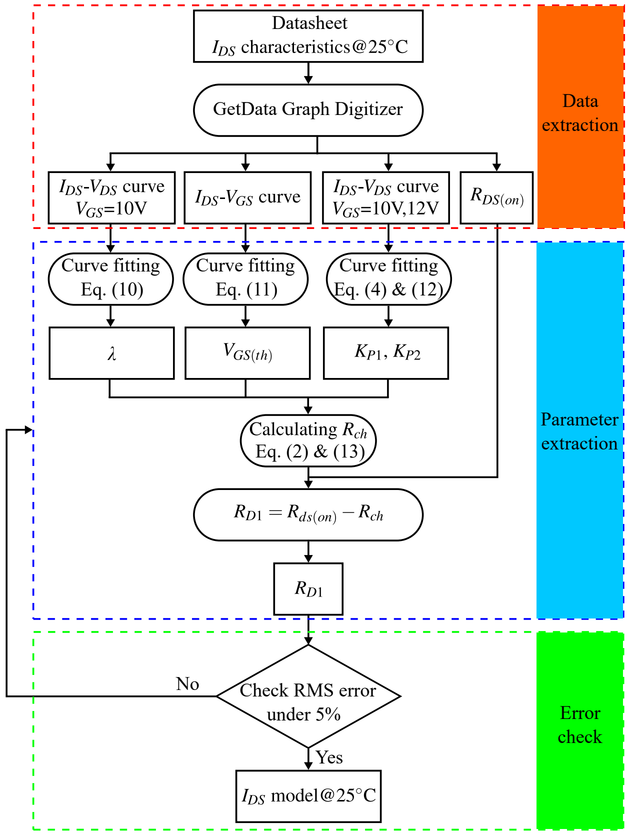

Figure 4: Modelling approach of I_{DS} at 25 °C.

Table 2: Parameters of I_{DS} at 25 °C.

K_{P1}	K_{P2}	$V_{GS(th)}$ (V)	R_{D1}(mΩ)	λ
4.886	0.2818	3.992	6.001	0.043

$I_{DS} = 120$ A. The channel voltage V_{ch} can be calculated under the same V_{GS} and I_{DS} condition according to (2). R_{ch} and R_{D1} can be then calculated as:

$$R_{ch} = \frac{V_{ch}}{I_{DS}} \tag{13}$$

$$R_{D1} = R_{DS(on)} - R_{ch} \tag{14}$$

5) RMS error check

After all the parameters are extracted, the accuracy of the model is checked by comparing the simulated $I_{DS} - V_{DS}$ characteristics with the characteristics of the datasheet. The root mean square (RMS) error is calculated using the following equation [2]:

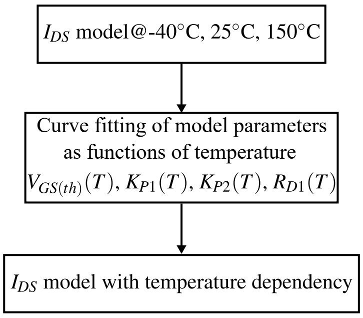

Figure 5: Modelling approach of I_{DS} with temperature dependency.

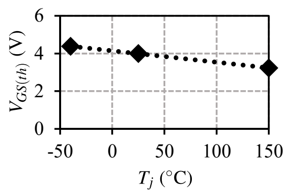

((a)) $V_{GS(th)}$.

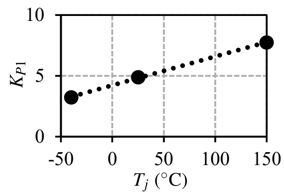

((b)) K_{P1}.

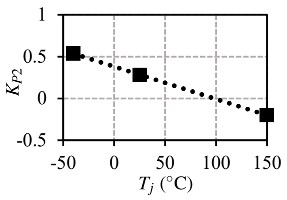

((c)) K_{P2}.

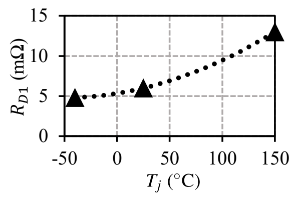

((d)) R_{D1}

Figure 6: Temperature dependency of model parameters.

$$RMS = \sqrt{\frac{\sum_{i=1}^{N} \mid m_i - s_i \mid^2}{N}} \times 100\% \tag{15}$$

where N, m_i and s_i denote the number of data, measured and simulated values of I_{DS}. If the calculated RMS error exceeds 5%, the parameter extraction procedure will be done again until the RMS error is lower than 5%.

The step-by-step modelling approach of I_{DS} is summarized in Fig. 4. The extracted parameters are shown in Table 2.

2.2.2 Modelling approach of I_{DS} with temperature dependency

In the datasheet of CAS120M12BM2, the I_{DS} characteristics at -40 °C, 25 °C and 150 °C are provided. They can be used to model the temperature dependency. The parameters K_{p1}, K_{p2}, $V_{GS(th)}$ and R_{D1} are modelled as linear or quadratic functions of temperature: $K_{p1}(T)$, $K_{p2}(T)$, $V_{GS(th)}(T)$ and $R_{D1}(T)$. Firstly, the parameters are extracted at different temperatures following the same approach shown in Fig. 4 . Secondly, the linear or quadratic functions are used to fit the values of each parameter at different temperatures. The modelling approach is summarized in Fig. 5. The temperature dependency of the parameters is shown in Fig. 6. The equations to describe the temperature dependency are:

$$\begin{cases} V_{GS(th)} = -0.006T + 4.1416 \\ K_{P1} = 0.0237T + 4.2227 \\ K_{P2} = -0.0039T + 0.3816 \\ R_{D1} = 0.0002T^2 + 0.0214T + 5.3409 \end{cases} \tag{16}$$

The comparison between the I_{DS} model with the datasheet is shown in Fig. 7. It can be seen that the simulated I_{DS} characteristics matches the datasheet very well, which can verify the effectiveness of the proposed modelling approach.

2.2.3 Modelling approach of diode

The diode model described in (6) and (7) contains two parameters that need to be extracted: R_{D2} and I_S. The parameters are extracted according to the diode characteristics available in the datasheet.

1) Series resistance R_{D2}

According to (6), the differential resistance of the voltage-dependent current source I_D can be calculated as:

$$R_D = \frac{\mathrm{d}V_D}{\mathrm{d}I_D} = \frac{kT}{q} \cdot \frac{1}{I_D + I_S} \tag{17}$$

According to (17), $R_D << R_{D2}$ can be assumed, when I_{DS} is larger than 100 A. Therefore, the slope of the diode characteristics in the high current linear region can be used to extract the series resistance R_{D2}.

2) Reverse saturation current I_S

After R_{D2} is extracted, the I_D–V_D characteristics can be obtained from the I_D–V_{SD} diode characteristics according to (7). I_S can be then extracted by fitting (6) to the I_D–V_D characteristics.

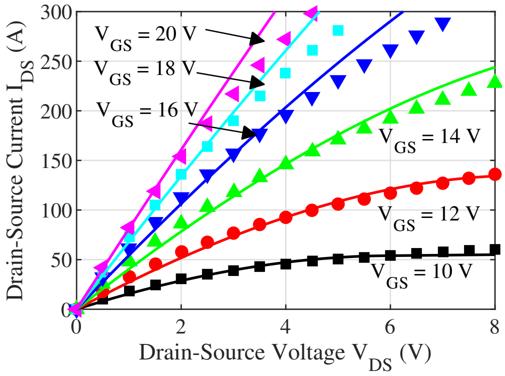

((a)) -40 °C.

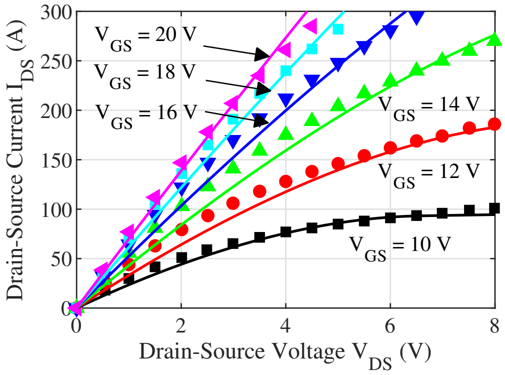

((b)) 25 °C.

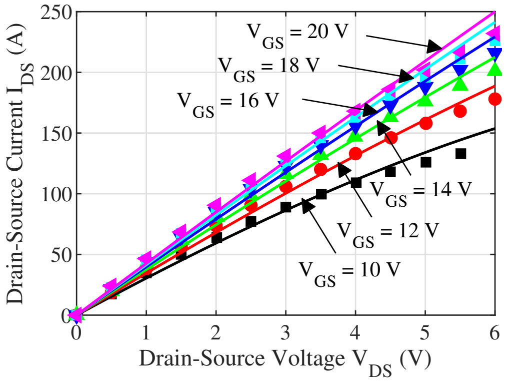

((c)) 150 °C.

Figure 7: I_{DS}–V_{DS} characteristics at different temperatures comparing to datasheet.

Table 3: Parameters of diode model.

I_S (A)	$R_{D2}(m\Omega)$
1.925e-14	4.66

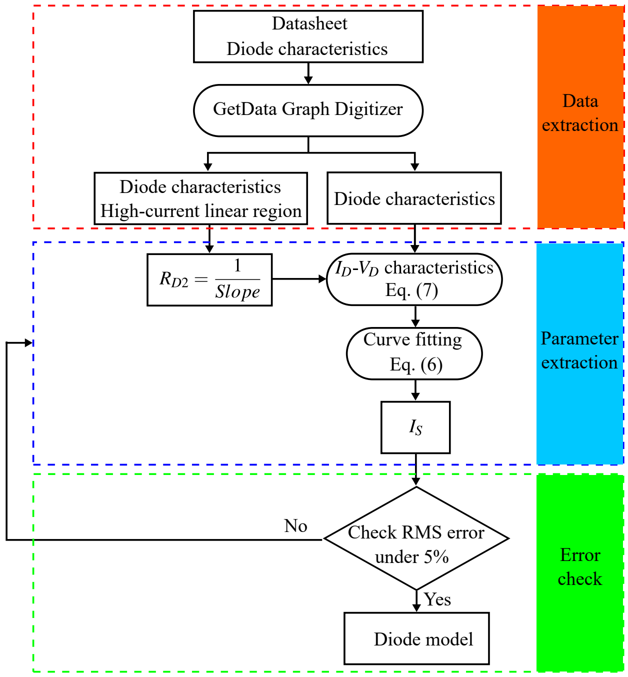

Figure 8: Modelling approach of diode.

The extracted parameters of the diode are listed in Table 3. The step-by-step modelling approach is summarized in Fig. 8. In Fig. 9, the diode model matches the diode characteristics in the datasheet very well, which can verify the effectiveness of the proposed modelling approach.

2.2.4 Modelling approach of parasitic capacitors

In the datasheet, the input capacitance C_{iss}, output capacitance C_{oss} and reverse transfer capacitance C_{rss} are given as the capacitance characteristics as shown in Fig. 10. C_{GS}, C_{GD} and C_{DS} can be calculated by C_{iss}, C_{oss} and C_{rss} according to (18):

$$\begin{cases} C_{GS} = C_{iss} - C_{rss} \\ C_{DS} = C_{oss} - C_{rss} \\ C_{GD} = C_{rss} \end{cases} \tag{18}$$

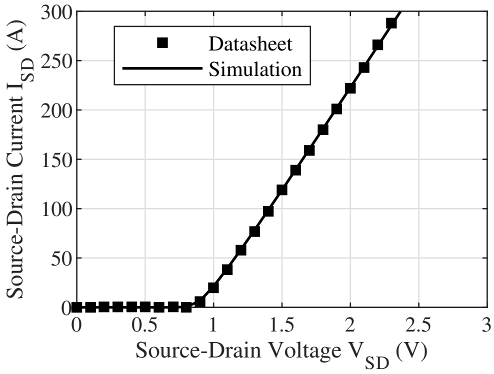

Figure 9: Diode characteristics comparing to datasheet.

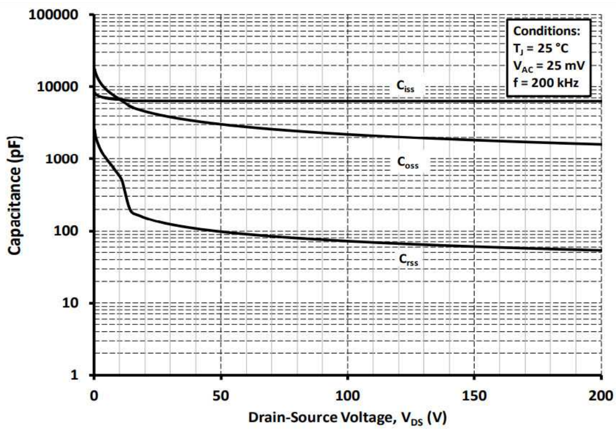

Figure 10: Capacitance characteristics of CAS120M12BM2 in the datasheet.

1) C_{GS}

A constant value is used to model C_{GS}. It can be easily extracted by subtracting C_{rss} from C_{iss} according to (18). $C_{GS} = 6319$ pF can be obtained for CAS120M12BM2.

2) C_{DS}

C_{DS} is a nonlinear capacitor varying with drain-to-source voltage V_{DS}. The C_{DS}–V_{DS} curve can be derived from the datasheet using (18). C_{DS0}, V_{bi}, M_{CDS} can be easily extracted by curve fitting using (8) and the C_{DS}–V_{DS} curve.

3) C_{GD}

C_{DS} is a more complicated nonlinear capacitor varying with drain-to-gate voltage V_{DG}. The C_{rss}–V_{DS} curve in the datasheet can be used to extract the parameters of C_{GD}. In Fig. 10, two significantly different slopes can be

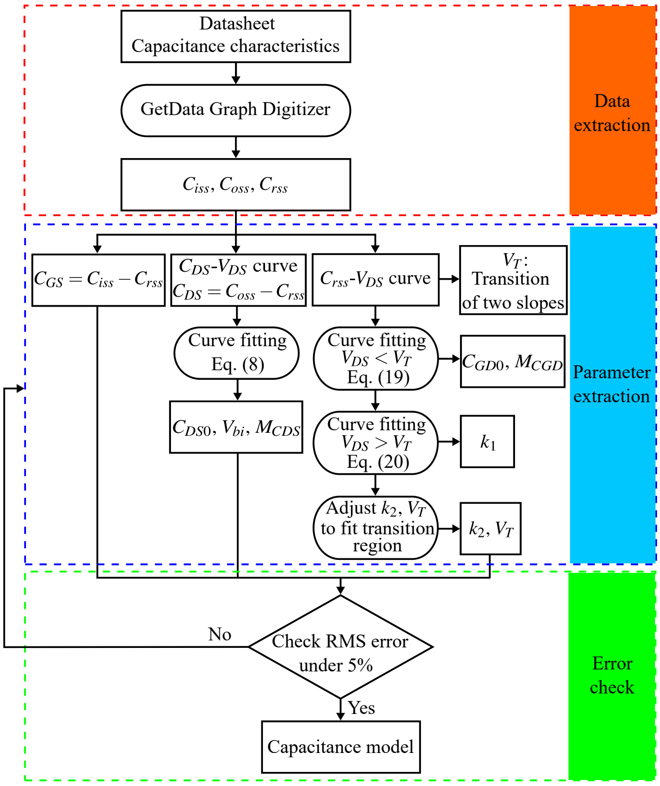

Figure 11: Modelling approach of parasitic capacitors.

observed in the C_{rss}–V_{DS} curve. V_T can be firstly extracted as the transition voltage of these two slopes. In (9), a hyperbolic tangent function is used to model the transition of slopes in C_{rss}–V_{DS} curve . When $V_{DG} < V_T$, (9) can be approximated as:

$$C_{GD} = \frac{C_{GD0}}{(1 + V_{DG})^{M_{CGD}}} \tag{19}$$

C_{GD0} and M_{CGD} can be extracted by curve fitting to fit (19) to C_{rss}–V_{DS} curve when $V_{DS} < V_T$.

When $V_{DG} > V_T$, (9) can be approximated as

Table 4: Parameters of capacitance model.

C_{GS}(pF)	C_{DS0}(pF)	V_{bi} (V)	M_{CDS}	C_{GD0}(pF)
6319	15500	1.622	0.478	2646
V_T(V)	k_1	k_2	M_{CGD}	
13.52	40.51	0.3815	0.4295	

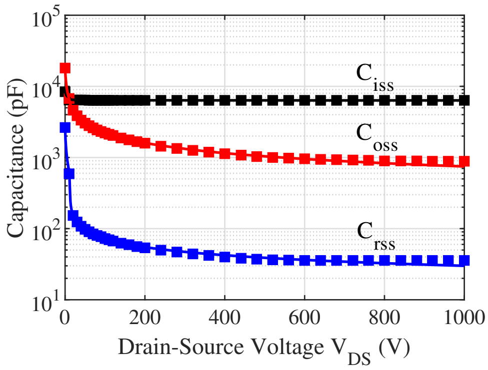

Figure 12: Capacitance characteristics comparing to datasheet.

$$C_{GD} = \frac{C_{GD0}}{\left(1 + V_{DG}\left(1 + k_1\right)\right)^{M_{CGD}}} \tag{20}$$

k_1 can be extracted by curve fitting to fit (20) to C_{rss}–V_{DS} curve when $V_{DS} > V_T$.

Finally, k_2 and V_T are adjusted to accurately fit the transition region of two different slopes of the C_{rss}–V_{DS} curve.

The step-by-step modelling approach of parasitic capacitors is summarized in Fig. 11. The extracted parameters are listed in Table 4. The comparison between the capacitance model and the datasheet is shown in Fig. 12, which shows a good agreement.

2.3 Model verification

A SPICE model is built for CAS120M12BM2B using the subcircuit model and extracted parameters. Both experimental platform and simulation platform of double pulse tester (DPT) are built to verify the proposed SPICE model. The experimental platform of DPT is shown in Fig. 13(a). A PCB board with low parasitic inductance is designed as the main circuit. A commercial gate driver CGD15HB62P1 for half-bridge module from Wolfspeed is used [12]. The upper switch is always off and the lower switch is controlled by the DPT signal generated by the DSP control board. A 55.7 μH with low equivalent parallel capacitance is designed as the load inductor. The equivalent series resistance of the load inductor is measured as 0.064 Ω. The voltage and current of the lower switch is measured by high-bandwidth differential voltage probes and high-bandwidth current probes.

The same simulation circuit of DPT is built in PSpice as shown in Fig. 13(b). The 5 nH DC-bus stray inductance is obtained by simulating the S-

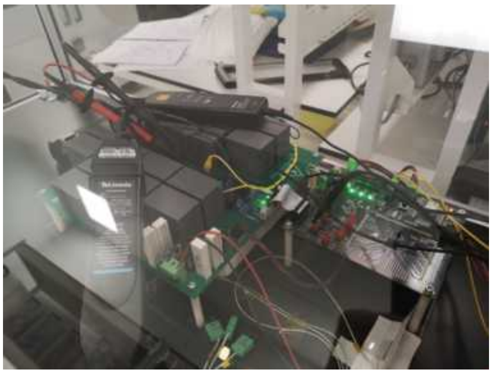

((a)) Experimental platform.

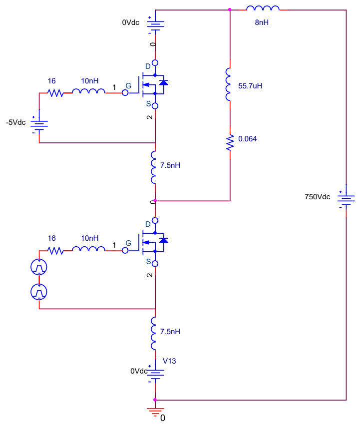

((b)) Simulation circuit.

Figure 13: Experimental platform and simulation circuit of DPT.

parameter of the PCB board including all the stray inductance of the DC capacitors in Keysight Advanced Design System (ADS) [13]. The stray inductance in the power module is 15 nH according to the datasheet. Two 7.5 nH inductors are added to the drain terminals of upper and lower SiC MOSFETs in the half-bridge module respectively to represent this stray inductance. The gate loop resistance is obtained by calculating the time constant of the measured gate-to-source voltage. The DPT results in both simulation and experiment are shown in Fig. 14 and Fig. 15. The simulation of the turn-on and turn-off transients shows good agreement with the experiment.

2.4 Toolbox to model SiC MOSFETs

Based on the aforementioned model and parameter extraction method, the model parameters, equations, required data inputs, and modelling steps can

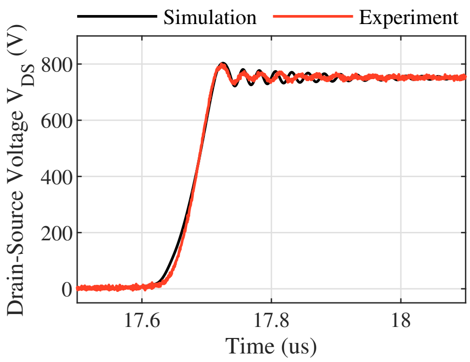

((a)) Turn-off voltage V_{DS}.

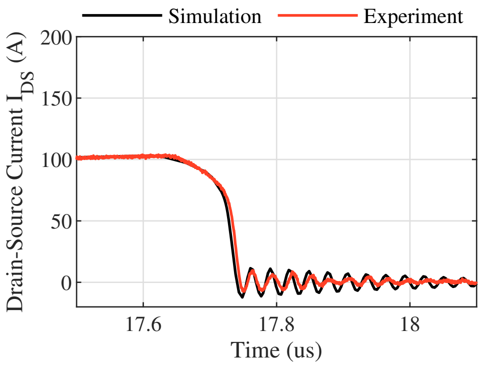

((b)) Turn-off voltage I_{DS}.

Figure 14: Comparison of turn-off waveforms by simulation and experiment at 25 °C.

be summarised as:

- 25 model parameters:
  - 5 parameters for drain-to-source current model: $\beta_0, VC, V_{GS,th}, R_{D1}, \lambda$
  - 9 parameters for temperature characteristics
  - 2 parameters for diode model
  - 9 parameters for parasitic capacitance model
- 16 equations divided in:
  - 5 equations for Drain-to-source current model: (1), (2), (3), (4), (5)
  - 4 equations for temperature characteristics: (16)

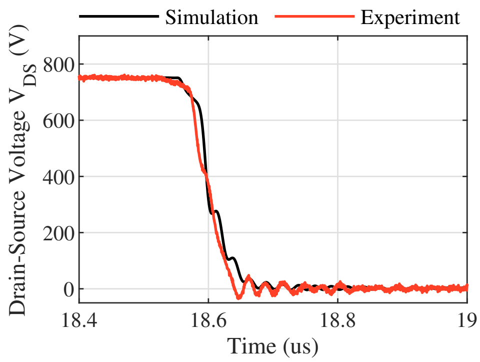

((a)) Turn-on voltage V_{DS}

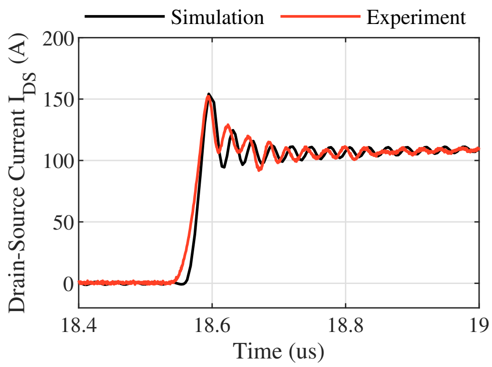

((b)) Turn-on voltage I_{DS}

Figure 15: Comparison of turn-on waveforms by simulation and experiment at 25 °C.

- 2 equations for diode model: (6), (7)
- 5 equations for parasitic capacitance: (8), (9), (18)

The SiC MOSFET model will require the following data inputs to extract the parameters:

- transfer characteristics under different temperature
- output characteristics under different temperature
- $R_{ds(on)}$
- diode characteristics
- capacitance characteristics

The curve fitting toolbox is used to extract the parameters of the model using the data from datasheet. The procedure of parameter extraction is described as:

1. Curve fitting of transfer characteristics and output characteristics to obtain the drain-to-source current model under different temperatures.
2. Curve fitting of temperature parameters to obtain the temperature characteristics.
3. Curve fitting of the diode characteristics to obtain the diode model.
4. Curve fitting of the capacitance characteristics to obtain the parasitic capacitance model.

This step-by-step modelling approach can be adopted as a toolbox in order to obtain a model for various SiC MOSFETs and power modules. The model developed by this toolbox can be further used for simulation, analysis and design of power electronics converters such as DC transformers.

3 Toolbox to design voltage controller of DC transformers

3.1 Transfer function of DC transformer

The voltage controller is designed for a DC transformer based on dual active bridge (DAB), as shown in Fig. 16. The main parameters of the DC transformer are summarized in Table. 5. Single phase shift modulation is used to control the DC transformer. The small signal model of DAB can be obtained according to [14]:

$$\hat{I}_{out} = \frac{nV_{in}}{f_{sw}L_{lk}}\hat{\varphi} \tag{21}$$

where φ is the phase shift angle between the ac voltages of the secondary and primairy side of the transformer.

The PI controller is used to control the output voltage of the DC transformer:

$$PI(s) = K_p \cdot (1 + \frac{1}{s\tau_i}) \tag{22}$$

where K_p and τ_i are the proportional gain and integral time constant of the PI controller. The closed-loop control diagram of the DC transformer is drawn in Fig. 17. The open loop transfer function can be written according to Fig. 17 as:

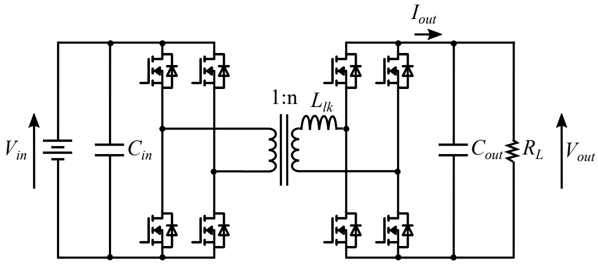

Figure 16: DC transformer based on DAB.

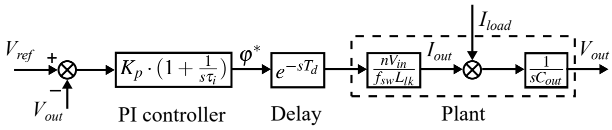

Figure 17: Control diagram of DC transformer.

$$H(s) = K_p(1+\frac{1}{s\tau_i})e^{-sT_d}\frac{nV_{in}}{f_{sw}L_{lk}}\frac{1}{sC_{out}} = \frac{K_p n V_{in}(1+s\tau_i)e^{-sT_d}}{s^2\tau_i f_{sw}L_{lk}C_{out}} \tag{23}$$

where e^{-sT_d} is used to represent the control delay and PWM delay.

Input Voltage (V_{in})	750 V
Output Voltage (V_{out})	50 V
Input Capacitor (C_{in})	1 mF
Output Capacitor (C_{out})	1 mF
Load resistor (R_L)	20 Ω
Leakage Inductance (L_{lk})	27.2 μH
Transformer ratio ($n=\frac{V_{out}}{V_{in}}$)	1/15
Switching frequency (f_{sw})	20 kHz
Control frequency (f_c)	10 kHz

Table 5: Parameters of DC transformer.

3.2 Controller design

The PI controller is designed according to the frequency response of the open loop transfer function of DC transformers. The phase margin and crossover frequency of the open loop transfer function are defined as ϕ_m and ω_c. The following equations are fulfilled at the crossover frequency:

$$\angle H(j\omega) = -\pi + \phi_m \tag{24}$$

$$\left|\angle H(j\omega_c)\right| = 1 \tag{25}$$

According to (23), the phase angle of the open loop transfer function can be calculated as:

$$\angle H(j\omega) = \arctan(\omega_c\tau_i) - \pi - \omega_c T_d \approx -\frac{\pi}{2} - \omega_c T_d \tag{26}$$

where $\arctan(\omega_c\tau_i) \approx \frac{\pi}{2}$, assuming $\omega_c\tau_i \gg 1$. The crossover frequency can be calculated according to (24) and (26):

$$\omega_c = \frac{\frac{\pi}{2} - \phi_m}{T_d} \tag{27}$$

The integral time constant of PI controller can be calculated to ensure $\omega_c\tau_i \gg 1$:

$$\tau_i = \frac{10}{\omega_c} \tag{28}$$

According to (23), the gain of the open loop transfer function at crossover frequency can be calculated as:

$$\left|\angle H(j\omega_c)\right| = \frac{K_p n V_{in}\sqrt{1+\omega_c^2\tau_i^2}}{\omega_c^2\tau_i f_{sw} L_{lk} C_{out}} \approx \frac{K_p n V_{in}}{f_{sw} L_{lk}\omega_c C_{out}} \tag{29}$$

The gain of the PI controller can be calculated according to (25) and (29):

$$K_p = \frac{f_{sw} L_{lk}\omega_c C_{out}}{n V_{in}} \tag{30}$$

3.3 Validation

Due to COVID-19, the laboratory of the university is now closed, so experimental validation cannot be provided. Instead, simulation is conducted to validate the designed voltage controller of DC transformers. The DAB-based DC transformer as shown in Fig. 16 is built in Simulink/Matlab. The parameters of the simulation model is shown in Table 5. According to (28) and (30), the integral time constant and proportional gain of the PI controller can be designed as:

$$\tau_i = 0.0014s \tag{31}$$

$$K_p = 0.076 \tag{32}$$

The simulation results are shown in Fig. 18. It can be seen that the output voltage of DC transformer can be controlled to follow the reference in a fast and accurate way.

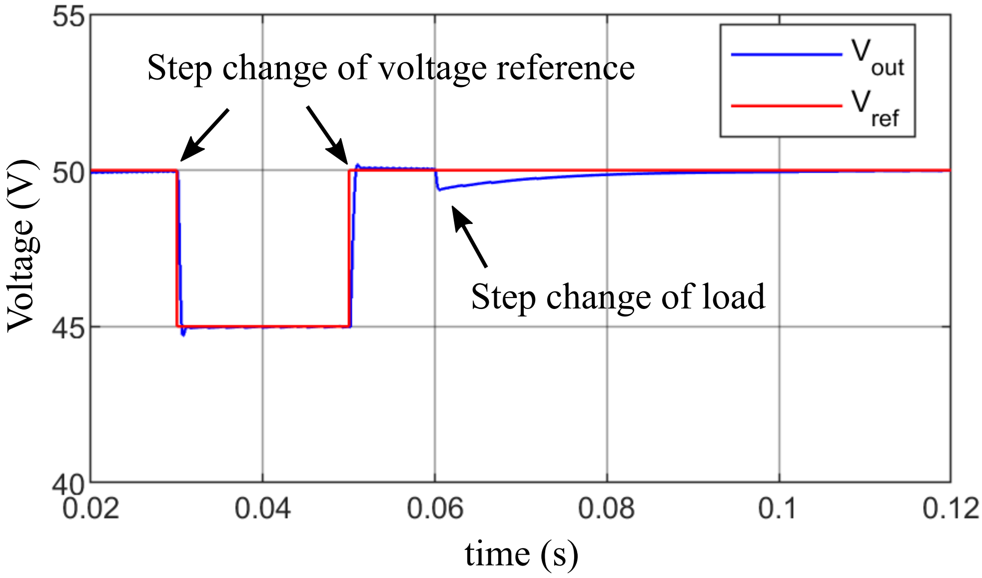

Figure 18: Simulation results of DC transformer.

3.4 Toolbox to design voltage controller of DC transformers

Based on the aforementioned modelling and controller design of DC transformers, the toolbox to design the voltage controller of DC transformers is summarized as follows:

- 9 model parameters listed in Table 5.
- 3 equations to calculate the parameters of PI controller:
  - equation to calculate the crossover frequency: (27)
  - equation to calculate the integral time constant: (28)
  - equation to calculate the proportional gain: (30)

The toolbox can be used to calculate the parameters of the voltage controller of the DC transformer.

4 Power SCADA/EMS Systems

The need for a supervisory and control tool was and still is required as the industrial revolution keeps evolving. The Supervisory, Control and Data Acquisition (SCADA) system is a combination of hardware parts containing sensors, actuators, communication medium, Input/Output (I/O) devices and Human Machine Interface (HMI). Additional to the software part that contains the server-side operating system, communication protocols, HMI applications and the terminal controller's interface are needed [15, 16, 17]. The evolution of the SCADA/Energy Management Systems (EMS) is presented in Table 6. Nowadays SCADA server-side can handle a complicated and powerful operating system (e.g. Windows server 2012), and Remote Terminal Unit (RTU)s can handle embedded operating systems. Such an expansion of software capability allows for testing and virtual scenarios simulation in the SCADA server-side before executing commands or procedures [15, 17, 18, 19].

Table 6: The historical evolution of SCADA

Year	Used Name
1890s	Remote Control and Remote Indication.
1920s	Telecommand and control.
1930s	Check Before Operate, Electro-Mechanical systems.
1960s	Supervisory Control Systems
1960s	Data Acquisitions - SCADA started to evolve.
1980s	Load Dispatch Centre and Control
1990s	Energy Control Centre
2000s	Energy Management Systems

SCADA today covers three different management systems: Business Management System (BMS), EMS and Generation Management System (GMS) [19].

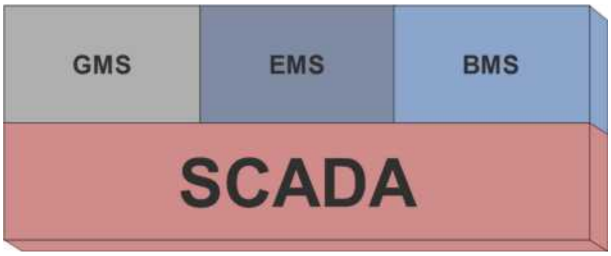

Figure 19: SCADA and different management systems

4.1 SCADA Components and Structure

A traditional SCADA system usually has the following components:

4.1.1 Operator Room station

The operations room of the SCADA system is one of the most important system components. Inside the room, there is a user interface unit called an HMI which provides a visual presentation of the hardware and the software components along with the communication medium. The specification of the HMI depends mainly on the network structure needs, some are specifically designed to be rigid, while others Commercial Off-The-Shelf (COTS) SCADA systems are more flexible and compatible with several installed hardware and software [16, 18, 20].

The HMI provides several services to the operators, that include [21, 22]:

1. Visually presenting the hardware, software and communication SCADA components. Very familiar shapes are used to help the operators such as green light for “OK” state, red light for “Alarm”.

2. Offering many operational functions to control the Master Terminal Unit (MTU)s, RTUs and Programmable Logic Controllers (PLC).

3. Presenting analog and digital I/O devices values. Sometimes, analog measurements are presented in gauges or bars to show the minimum and the maximum allowed values, e.g. the voltage level of a substation or bus.

4. An alarm system that detects and acts according to several alarms scenarios. These scenarios can be automated actions such as pre-programmed safety procedures, or just indicators and events that inform the operators about the case through emails or text messages.

4.1.2 Communication Infrastructure

The communication infrastructure of the SCADA system is considered a challenge because it depends mainly on the coverage area, material and protocols. Different technologies have been already used in the SCADA field such as radio wave, serial modems, Local Area Network (LAN)/Wide Area Network (WAN) and Transmission Control Protocol (TCP)/Internet Protocol (IP) over Synchronous Optical Networking (SONET) [16, 17, 19]. The communication monitoring network has different topologies, such as Point to Point (PTP), Point to Multiple (PTM), and Multiple to Multiple (MTM). For large scale SCADA, fiber optic, satellite and microwaves technologies are usually used as a communication medium [23, 24].

SCADA uses different types of communication protocols; some of them are operated on on-demand mode only (send data by request). These protocols include RP-570, RS-485, Modbus, Profibus and Conitel. In addition, several protocols standards are available, e.g. International Electro Technical Commission (IEC) 60870-5-101/104, IEC 61850 and Distributed Network Protocol (DNP3) [21, 25]. According to these standards, some of the protocols can deal with TCP/IP, which provides higher security. However, it is always recommended that SCADA system should not be connected to the internet to avoid any DOS or cyber attacks. In 1996, Object Linking and Embedding for process control (OLE PC) was developed, which allowed real-time data communication between different terminals manufacturers, RTUs and MTUs [24, 26].

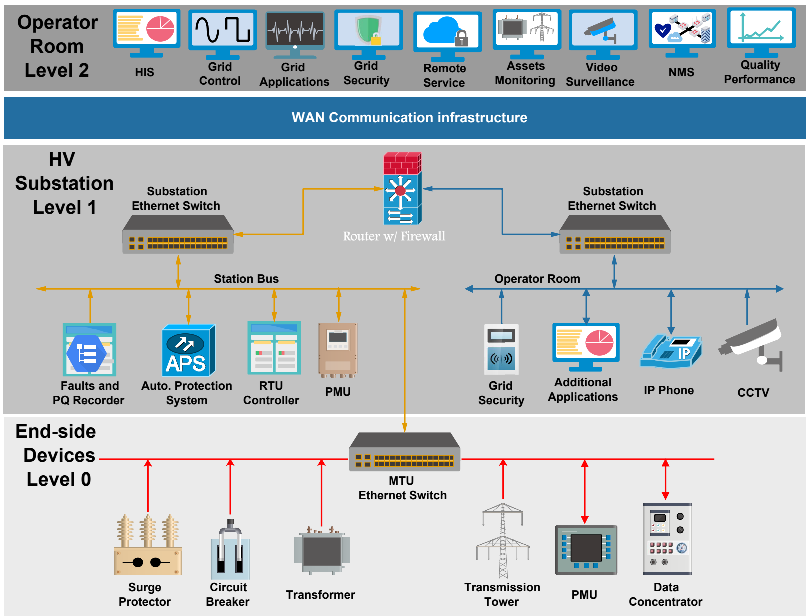

Figure 20: SCADA in HV Transmission Network

The SCADA communication network has gone through several generations depending on the size and number of connected equipment. These generations, in order, are Monolithic, Distributed, Networked and Internet of Things (IoT) [23, 27, 28]. The SCADA communication network for a transmission network can be divided into three levels as shown in Figure 20. A complete modern power network from generation to demand is shown in Figure 21 [19].

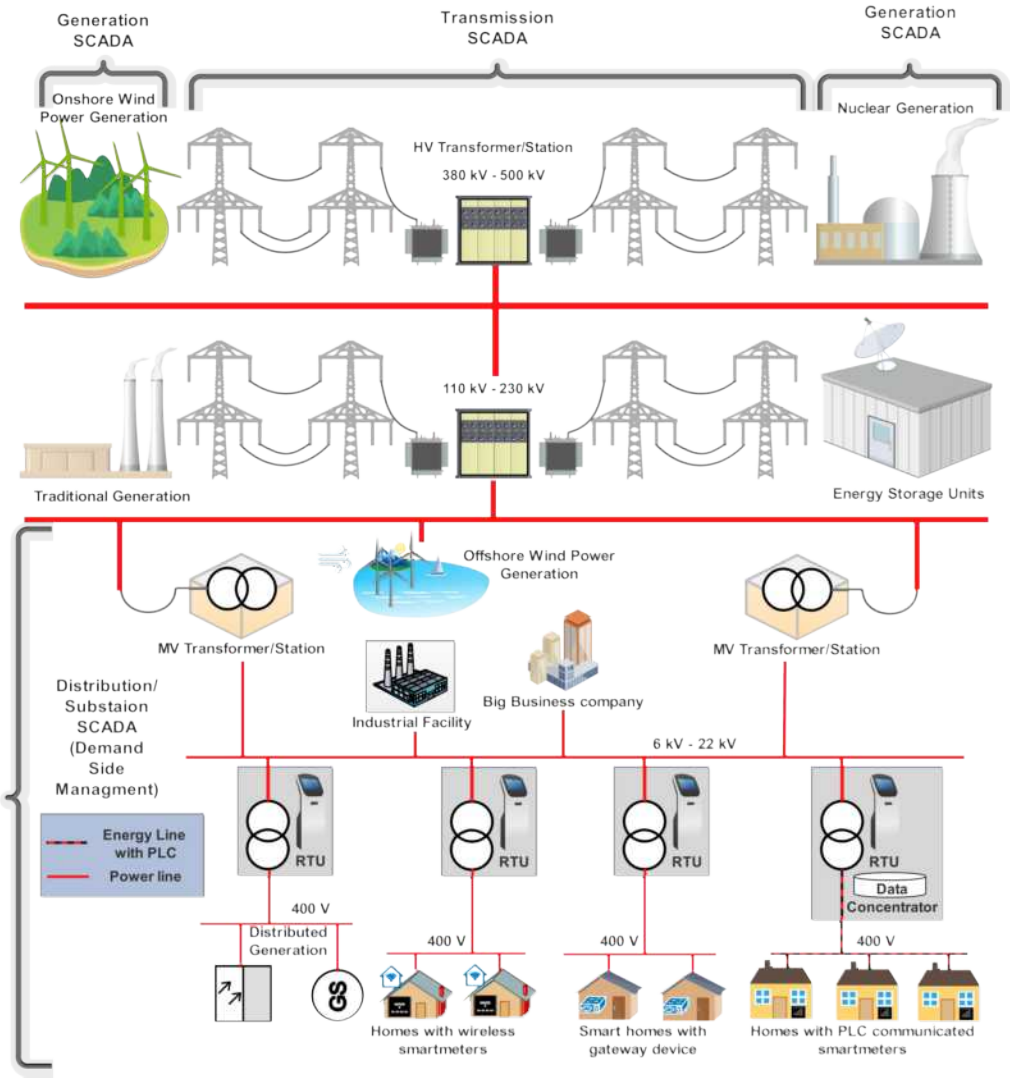

Figure 21: Modern power system from generation to demand

The distribution network has more nodes than the HV transmission network with more unbalanced voltage magnitudes. As a result, the communication network is a big challenge for a robust SCADA [25]. There are various topologies of communication infrastructure available as shown below [16, 17, 22, 23]:

- **Fiber Optics**

  Fiber optics are very compatible with medium and low voltage distribution networks as shown in Figure 22. Deployment cost of this technology is considered high due to the related civil works and expensive equipment. However, fiber optics technology provides robustness, noise-free, wide data bandwidth and extendable communication medium.

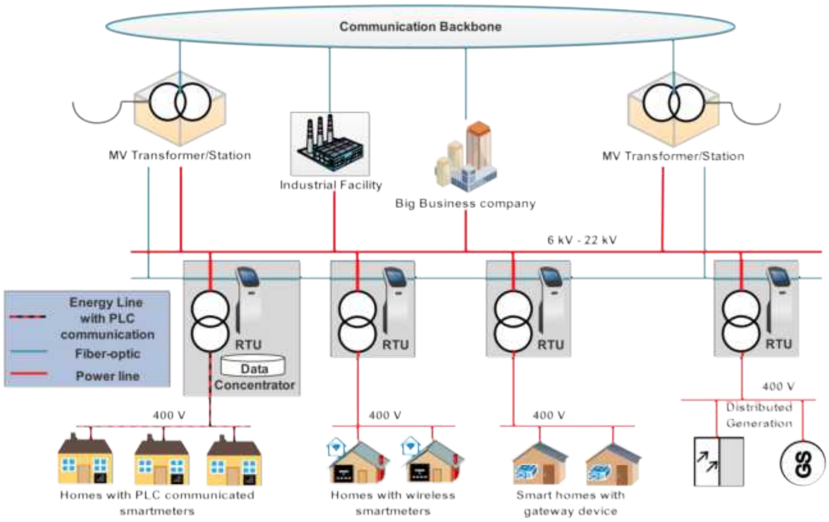

Figure 22: SCADA communication infrastructure: Fiber Optics topology.

- **Power Line Carrier communication**

  Power Line Carrier communication (PLCC) has an advantage of its compatibility with the traditional power grid, no need for new assets or structures. Therefore, it is considered the joker solution whenever no other option is available. However, the quality of the communication (range and bandwidth) depends mainly on the type and age of the cables, in addition to the number of joints. As a consequence, accurate planning of the engineering installation of the PLCC units is needed to guarantee low latency, reliable connection, and stable data metering.

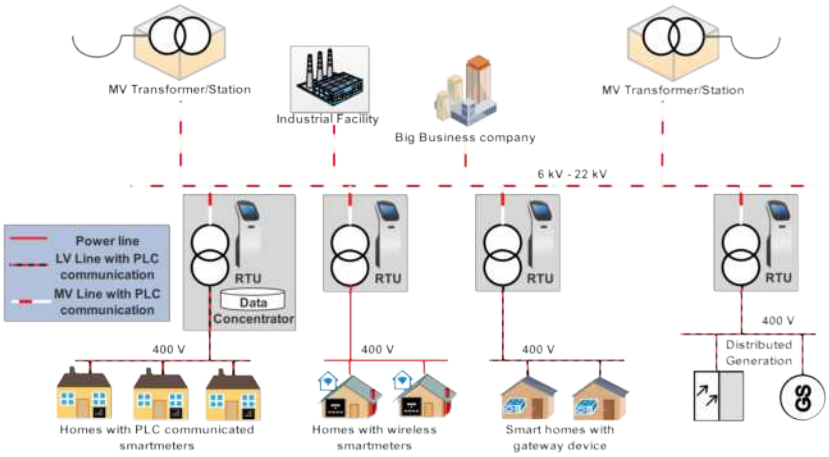

Figure 23: SCADA communication infrastructure: PLCC topology.

- **WiMax and LTE**

  WiMAX (Worldwide Interoperability for Microwave Access) or LTE (Long-Term Evolution) technology, both are used in power system communication to connect lower networks with higher ones through the backhauling mechanism. Usually, lower networks contain RTUs and data concentrators. This communication medium allows local networks to communicate with regional networks privately.

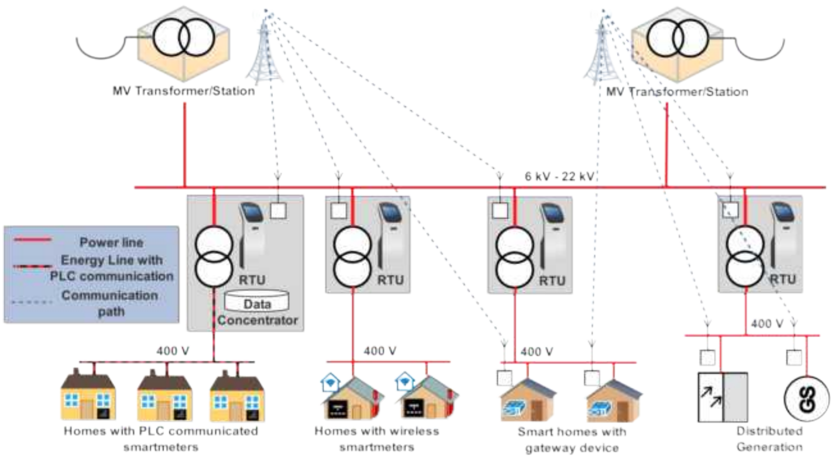

Figure 24: SCADA communication infrastructure: WiMAX topology.

4.1.3 Master and Remote Terminal Units

- Master Terminal Units MTUs

MTUs are considered the second control unit (Level 1) after the main station (Level 2), and are usually installed in substations [17]. MTUs have similar characteristics of the main station, like HMI, servers and they are connected to other MTUs through a communication medium, e.g. LAN/WAN. The HMI allows the operators to control the connected RTUs through predefined procedures and some visual presentation of geographical and textual information and shapes. This content is usually easy to understand by the MTU operators [21, 29].

- Remote Terminal Units RTUs

  RTUs are considered the slaves of the master station and MTUs. RTUs are more advanced than PLCs and considered an extended version of them. They contain sensors, actuators and a controller unit, they work in real-time and are synchronized with the network. They can transmit data to the master terminal in periodic behavior or on-demand requests [17, 30]. Also, RTUs have some predefined emergency procedures to send signals and data to the master station in high priority in case of disasters or high-risk faults [19, 21].

  RTUs are geographically distributed, usually with Global Positioning System (GPS) modules installed to label time to the measurements (time-synchroniser). The communication medium is considered a LAN/WAN link and several technologies can be employed such as radio, fiber optic, telephone wires, and microwaves [17, 21]. Usually, the standard of functional block programming IEC 61131-3 is used to build up PLCs and RTUs programs [19, 21, 22].

4.2 SCADA/EMS Functions, Managements and Toolboxes

There are multiple functions/toolboxes for SCADA/EMS as shown in the following sections:

4.2.1 Operations Management

Operation management is the main core of the system; it includes several components and sub-functions, which can be listed as follow [17, 19, 22]:

- SCADA Engine;
- Dynamic Network Model;
- Historic Information System (HIS);

- Statistics, Reports and Alerts;
- Technical Supervision.

The SCADA core contains all data and commands processes including the associated hardware needed. The core engine is a complex computer processor that performs all data and control commands, executes the sequencing process, and supports interface with multiple slaves (sub-processors) [17, 21]. Usually, there is a switched-on standby redundancy for the core. The processor is responsible for all data transfer, logging and running condition recording. Usually, an alarm system is integrated with it.

The alarm system is a package that receives signals from different sources, filters them and executes the suitable procedures, such as launching a siren, blinking red lights and/or sending an SMS notification. A printer and visualisation management system is integrated with the core, and it is responsible for providing a visual presentation of the network, hardcopy and softcopy. The system generates diagrams and schematics based on geographical sources [15, 19, 21].

The dynamic network model is an object hierarchical model that is based on the geographical representation of the network, taking into account the resources, assets and connectivity of the network . It is considered dynamic due to the online and continuously changing visualisation of the asset's status's. A supervision layer over this network allows operators to execute new actions on the network [15].

The HIS is mainly responsible for data logging and managing the database/ storage from RTUs, errors, alarms, diagnostic debugging, and user actions. HIS is used in many other SCADA functions, such as forecasting, event analysis or comparing, and for operator training case studies [21].

The report and alert module provides Real-time and historical reports for all SCADA functions and partitions. The module exports reports in many forms, including SMS, emails, PDF or diagrams [21].

4.2.2 Power Application Software (PAS)

SCADA PAS provides optimal management of electrical network from generation through transmission and distribution. In PAS, the safety of the network is a priority, and it can be maintained through full automation and support of the operational conditions and network optimisation. All the functions are connected to all the SCADA sectors, for example, data or load profile from the HIS increases the accuracy of the state estimation function. Usually, PAS is deployed in multi-server scalable architectures [21, 26].

There are four main categories of the PAS functions:

1. Analysis and Optimization Management: it focuses mainly on the optimization of energy dispatch under security and economical constraints. Also, it provides system stability analysis and load modelling, which are used by other SCADA management systems such as the forecasting and the state estimations algorithms. This management mainly provides the following functions [17, 19, 21]:
   - Load Profile Modelling;
   - Short Circuit Analysis;
   - Optimal Power Flow (OPF) and Distribution Optimal Power Flow (DOPF);
   - Voltage/VAr Control (VVC);
   - Contingency Analysis (CTA);
   - Voltage Stability Analysis;
   - Watershed Management.
2. Automation Management: provides network stability supervision and measurement monitoring. It supervises the system states over the power network, and monitors all the equipment that can lead to unstable operation conditions during faults or outages. The main toolboxes of the automation management can be listed as follow [17, 19, 22, 31]:
   - State Estimator, Load allocation and Power Flow;
   - Monitoring and controlling outages; executing recovery procedures;
   - Monitoring of CO2 Emissions and Fuel Reserve.
3. Operational Management: deals with all outages, faults and provides the optimal procedure for fast and safe restoration. The FDIR is a system that generates and executes a switching order when a fault has occurred to isolate the fault. Afterwards, the operators can take further safety precautions for manual execution, usually electronically dispatched. The operational management contains many toolboxes, but the most used ones are [17, 19, 21, 22]:
   - Fault Detection, Location, Isolation and Reconfiguration (FDIR);
   - Automatic Generation Control (AGC) with load frequency control;
   - Load Shedding and Scheduling.

4. Forecast Management: uses the data provided from the HIS, to carry multiple forecasting procedures [17, 19, 21, 22], such as :
   - Short-term Load Forecast;
   - Wind Speed/Direction Forecast;
   - Renewable Generation Forecast.

5 The Unified WLS State estimator toolbox

5.1 Weighted Least Squares (WLS) algorithm

The state estimation toolbox focuses on determining the system states using the maximum available measurements from the grid. However, it requires some pre and post-processing stages, as shown in Figure 25. The pre-processing stages include observability analysis (measurements, network model and circuit breakers states), while the post-processing includes bad data detection and elimination processes [32, 33, 34].

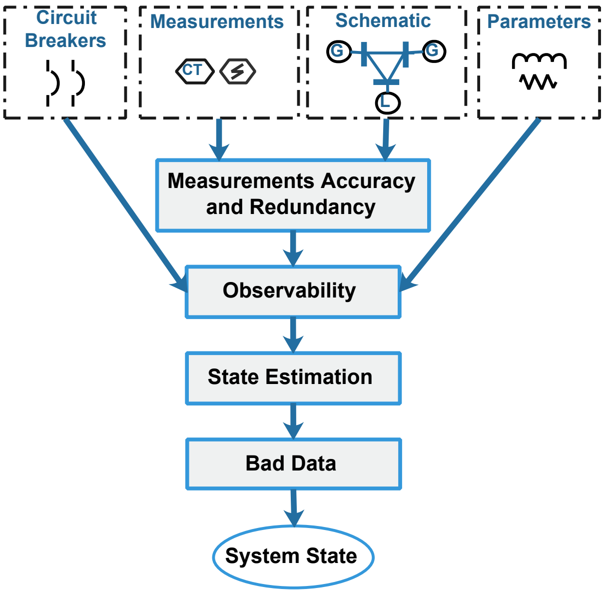

Figure 25: State estimation stages.

The state estimator aims to reduce or eliminate the errors in the collected measurements from the network to achieve the closest possible estimates of the system states. It assumes that the system measurements are corrupted (noisy) with error e as shown in the equation below:

$$z = h(x) + e \tag{33}$$

The WLS state estimation algorithm is commonly used in SCADA and EMS. It aims to minimize the square error (residual r) of the measurements by solving the following minimizing objective function:

$$WLS_{obj}(x) = \sum_{i=1}^{n} \frac{r_i^2}{{\sigma_i}^2} = \sum_{i=1}^{n} \frac{\big(z_i - h_i(x)\big)^2}{{R_{ii}}^2} \tag{34}$$

where, $z = \begin{bmatrix} z_1 & z_2 & \dots & z_n \end{bmatrix}^T$ is the measurements vector with n measurements, x is the state variable vector, $h(x) = \begin{bmatrix} h(x)_1 & h(x)_2 & \dots & h(x)_n \end{bmatrix}^T$ is a vector of nonlinear equations evaluated at the state variable x, e is the error (assumed to be Gaussian noise), and R_{ii} is a diagonal matrix that contains all measurements variances, $R_{ii} = \text{diag} \begin{bmatrix} \sigma_1^2 & \sigma_2^2 & \sigma_1^2 & \dots & \sigma_i^n \end{bmatrix}^T$ for independent measurements.

Equation (34) can be reformulated in matrix minimization form as follow:

$$\min_x WLS_{obj}(x) = \min_x \big(z - h(x)\big)^T R_{ii}^{-1} \big(z - h(x)\big) \tag{35}$$

The state variables x of an AC system with n buses are:

$$\begin{bmatrix} 0 & \theta_1 & \theta_2 & \dots & \theta_n; V_1 & V_2 & \dots \\ & V_n \end{bmatrix}^T; \tag{36}$$

the voltage angle of the slack (reference) bus (θ_1) is set to zero, and θ_n and V_n are the n^{th} bus phase angle and voltage magnitude respectively [34].

This minimization problem can be reformulated and solved using Taylor series and Newton-Raphson as explained in [35], which results with the following formulas:

$$\hat{x}_{k+1} = \hat{x}_k + \Delta\hat{x}_k \tag{37}$$

where $\Delta\hat{x}_k$ is the change/update on the system states, and calculated as follow:

$$\Delta\hat{x}_k = \big[G(\hat{x}_k)\big]^{-1} \nabla F(\hat{x}_k) \tag{38}$$

$$\nabla F(\hat{x}_k) = H^T(x_k) R_{ii}^{-1}(x_k)(z - h(x_k)) \tag{39}$$

$$G(x_k) = H^T(x_k) R_{ii}^{-1}(x_k) H(x_k) \tag{40}$$

where $G(x_k)$ is the Gain matrix and $H(x) = \frac{\partial h(x)}{\partial x}$ is the Jacobian matrix.

Equation (41) shows the complete formula for the system states updates ($\hat{x}_{k+1}$). The WLS estimation algorithm steps are shown in the figure 26 flowchart.

$$\hat{x}_{k+1} = \hat{x}_k + \left[H^T(x_k)R_{ii}^{-1}(x_k)H(x_k)\right]^{-1} \left[H^T(\hat{x}_k)\, R_{ii}^{-1}(x_k)\left(z - h\left(\hat{x}_k\right)\right)\right] \quad (41)$$

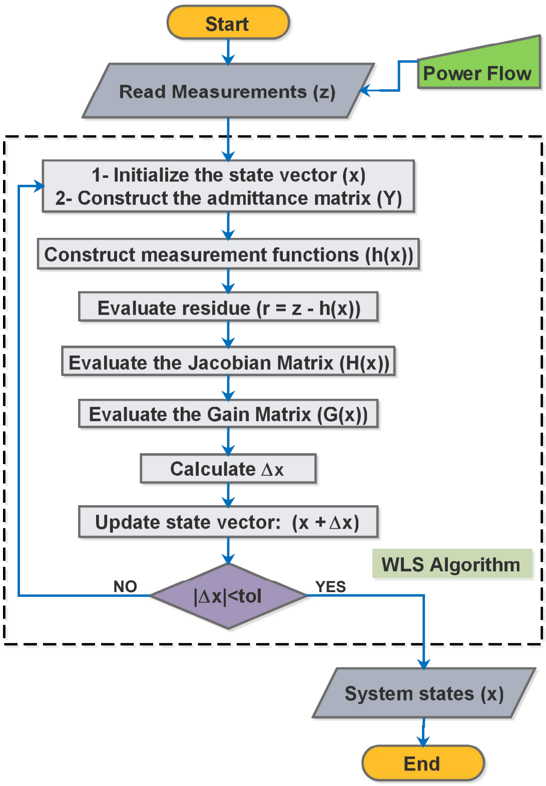

Figure 26: State estimation algorithm

5.1.1 AC Power flow calculations

The AC nonlinear measurement functions

$$h_{ac}(x) = [h_{ac_1}(x),\ h_{ac_2}(x),\ h_{ac_3}(x),\ h_{ac_4}(x),\ h_{ac_5}(x)] \quad (42)$$

are expressed as equations related to the current flow between buses, the power flow in the lines and the power injected into/from a bus [34]. These formulas can be categorized as follow:

1. $h_{ac_1}(x)$ and $h_{ac_2}(x)$ for active P_i and reactive Q_i power injection at bus i respectively:

$$h_{ac_1}(x) = P_i = \sum_{j\epsilon N_i} P_{ij} = V_i \sum_{j\epsilon N_i} V_j \left(G_{m_{ij}} \cos(\theta_{ij}) + B_{m_{ij}} \sin(\theta_{ij})\right) \quad (43)$$

$$h_{ac_2}(x) = Q_i = \sum_{j\epsilon N_i} Q_{ij} = V_i \sum_{j\epsilon N_i} V_j \left(G_{m_{ij}} \sin(\theta_{ij}) - B_{m_{ij}} \cos(\theta_{ij})\right) \quad (44)$$

2. $h_{ac_3}(x)$ and $h_{ac_4}(x)$ for active P_{ij} and reactive Q_{ij} power flow from bus i to j respectively:

$$h_{ac_3}(x) = P_{ij} = V_i^2 \left(G_{m_{ij}} + G_{sh_i}\right) - V_i V_j \left(G_{m_{ij}} \cos(\theta_{ij}) + B_{m_{ij}} \sin(\theta_{ij})\right) \quad (45)$$

$$h_{ac_4}(x) = Q_{ij} = -V_i^2 \left(B_{m_{ij}} + B_{sh_i}\right) - V_i V_j \left(G_{m_{ij}} \sin(\theta_{ij}) - B_{m_{ij}} \cos(\theta_{ij})\right) \quad (46)$$

3. $h_{ac_5}(x)$ for current flow I_{ij} from bus i to j:

$$h_{ac_5}(x) = I_{ij} = \frac{\sqrt{P_{ij}^2 + Q_{ij}^2}}{V_i} \quad (47)$$

If shunt admittance $(G_{sh_i} + jB_{sh_i})$ is ignored, then:

$$h_{ac_5}(x) = |I_{ij}| = \sqrt{\left(G_{m_{ij}}^2 + B_{m_{ij}}^2\right)\left(V_i^2 + V_j^2 - 2V_i V_j \cos(\theta_{ij})\right)} \quad (48)$$

where i and j are 'from' and 'to' buses respectively, V_i is voltage magnitude and θ_i is phase angle where $[\theta_{ij}] = \theta_i - \theta_j$, $(G_{m_{ij}} + jB_{m_{ij}})$ is the (i, j) element of the complex admittance matrix, $(G_{sh_i} + jB_{sh_i})$ is the i^{th} shunt admittance, N_i represents all the buses connected to bus i [34].

5.1.2 DC Power flow calculations

On the DC side, the measurement functions

$$h_{dc}(x) = [h_{dc_1}(x),\ h_{dc_2}(x),\ h_{dc_3}(x)] \quad (49)$$

are expressed as real power injection, power flow and current flow expressions as defined below:

1. $h_{dc_1}(x)$ for real P_i power injection at bus i:

$$h_{dc_1}(x) = P_i = \sum_{j \epsilon N_i} P_{ij} = V_i \sum_{j \epsilon N_i} V_j \left(pG_{m_{ij}}\right) \tag{50}$$

if droop control is used, the the real P_i power injection at bus i becomes:

$$h_{dc_1}(x) = P_{i_0} - \frac{1}{K_i}(V_i - V_{i_0}) \tag{51}$$

where,

$$p = \begin{cases} 1, & \text{for monopolar systems} \\ 2, & \text{for bipolar systems} \end{cases} \tag{52}$$

2. $h_{dc_2}(x)$ for real P_{ij} power flow from bus i to j:

$$h_{dc_2}(x) = P_{ij} = V_i^2 \left(pG_{m_{ij}} + G_{sh_i}\right) - V_i V_j \left(pG_{m_{ij}}\right) \tag{53}$$

3. $h_{dc_3}(x)$ for current flow I_{ij} from bus i to j::

$$h_{dc_3}(x) = I_{ij} = \frac{Pdc_{ij}}{Vdc_i} = pG_{m_{ij}}(V_i - V_j) \tag{54}$$

5.1.3 Converter Power coupling

The power relation between the AC and DC sides through the converter can be presented as follows [36]:

$$P_{ac} + P_{dc} + P_{convloss} = 0 \tag{55}$$

Where $P_{convloss}$ is the converter loss itself and can be calculated through experimental statistical approach based on Equation (56) and the current through the converter (I_c) [37, 38]:

$$P_{convloss} = a + b.I_c + c.{I_c}^2 \tag{56}$$

a, b and c are factors that depend on the converter type, operating condition and components (number of diodes, switches etc...). These values are represented as follow [36, 37]:

- a has a typical value of $11.033 \cdot 10^{-3} pu$ and it represents the no load losses of transformers and averaged axillary equipment losses, such as heating and cooling losses;

- b has a typical value of $3.464 \cdot 10^{-3} pu$ and it represents the switching losses of valves and freewheeling diodes;

- c represents the conduction losses of the valves and depends on the operating condition of the converter (rectifier or inverter). it's typical values are:

$$c = \begin{cases} 4.4 \cdot 10^{-3} pu, & \text{for rectifiers} \\ 6.67 \cdot 10^{-3} pu, & \text{for inverters} \end{cases} \tag{57}$$

In addition to the converter losses themselves ($P_{convloss}$), there are the AC side transformer, filter and reactor (Transformer, Filter and Reactor (TFR)) losses as shown in Figure 27. In this work, the TFR term is used to refer to these losses as part of the AC grid.

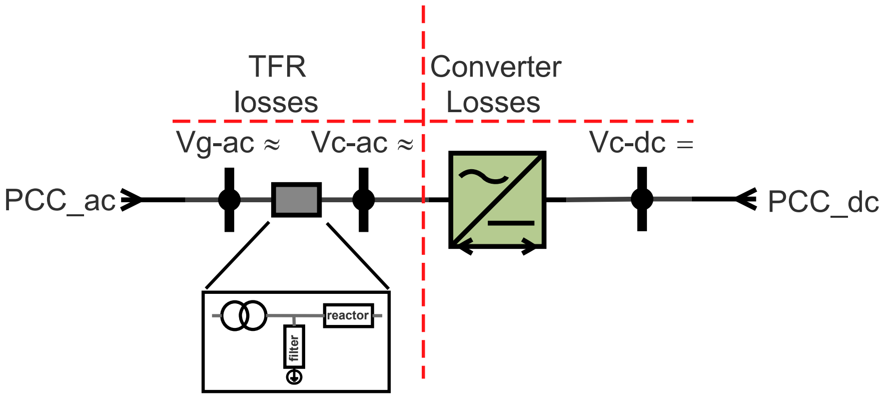

Figure 27: Converter power loss schematic

5.1.4 Converter voltage coupling

The converter can be dealt with as a transformer where the voltage levels on both sides are maintained by M_{factor} ratio (modulation index) as shown in Figure 28 [35, 39]. Considering that, if the converter can provide a ratio between the AC and DC sides voltages, then this extra information can be used as a redundant measurement in the state estimator.

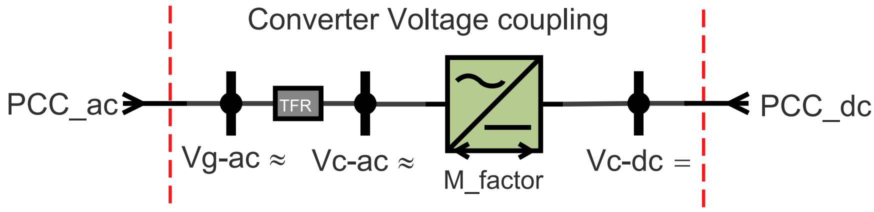

Figure 28: Converter voltage coupling

Let M_{factor} be a redundant measurement provided from the converter at the moment of measuring. Then the voltage relation between both sides of the converter is:

$$M_{factor} = K\frac{V_{c-dc}}{V_{g-ac}} \tag{58}$$

V_{g-ac} is calculated based on the converter current direction as shown below, where V_{TFR} is the TFR voltage drop.

$$V_{g-ac} = \begin{cases} V_{c-ac} + V_{TFR}, & \text{for rectifier} \\ V_{c-ac} - V_{TFR}, & \text{for inverter} \end{cases} \tag{59}$$

Equation (58) can be reformulated as an equality constraint in the WLS algorithm.

$$KV_{c-dc} - V_{g-ac}M_{factor} = 0 \tag{60}$$

where K is the voltage conversion factor, it can have different values based on the AC side network topology and converter type as shown in Equation (61).

$$K = \begin{cases} \frac{\sqrt{3}}{2\sqrt{2}}, & \text{see: [35]} \\ \frac{1}{\sqrt{2}}, & \text{see: [39]} \end{cases} \tag{61}$$

5.2 The Unified WLS for VSC HVDC/AC modifications

Considering the presented AC and DC side coupling approaches, a unified state estimator can be constructed. It is a single state estimator that solves one algorithm for the whole Voltage Source Converter (VSC)-HVDC/AC system together, using a single unified Jacobian matrix. The modified measurements input for the WLS is formulated below:

$$z = [zAC_1\ zAC_2 ... zAC_n | zDC_1\ zDC_2 ... zDC_m | zConv_1\ zConv_2 ... zConv_k | M_{factor_1}\ M_{factor_2} ... M_{factor_k}] \tag{62}$$

where

- zAC are the AC side measurements and can be in the form of Vm, Va, P_{inj}, $Q_{inj}, P_{flow}, Q_{flow}, I_{flow}$;
- zDC are the DC side measurements and can be in the form of Vm, P_{inj}, P_{flow}, I_{flow};
- $zConv$ are zero measurements and represent the right side of converter power coupling constraints;
- M_{factor} are the V_{dc} to V_{ac} ratios (measurements), calculated and transmitted by the converter;
- n, m and k are the number of AC systems, DC systems and converters respectively.

The measurement functions $h(x)$ in the unified WLS have the same format of the z vector.

The new Jacobian matrix is formatted in the following manner:

$$H_{unified}(x) = \frac{\partial h(x)}{\partial x} = \begin{bmatrix} H_{AC-AC} & H_{DC-AC} \\ H_{AC-DC} & H_{DC-DC} \end{bmatrix} \tag{63}$$

Which can be reformatted differently to simplify the structure as shown below:

$$H_{unified}(x) = \begin{bmatrix} H_{AC-AC} & 0 \\ 0 & H_{DC-DC} \\ H_{Conv-AC} & H_{Conv-DC} \\ H_{M-AC} & H_{M-DC} \end{bmatrix} \tag{64}$$

The expanded unified Jacobian matrix in (65) represents all hybrid VSC-HVDC/AC system components in one matrix. It includes the AC, DC and converter power and voltage coupling elements, and it is structured for n^{th} AC systems, m^{th} DC systems and k^{th} Converters.

$$H_{unified}(x) = \begin{bmatrix} H_{(AC-AC)_1} & 0 & 0 & ... & 0 & 0 & 0 \\ 0 & H_{(AC-AC)_2} & 0 & ... & 0 & 0 & 0 \\ 0 & 0 & H_{(AC-AC)_n} & ... & 0 & 0 & 0 \\ 0 & 0 & 0 & ... & H_{(DC-DC)_1} & 0 & 0 \\ 0 & 0 & 0 & ... & 0 & H_{(DC-DC)_2} & 0 \\ 0 & 0 & 0 & ... & 0 & 0 & H_{(DC-DC)_m} \\ H_{(Conv-AC)_1} & 0 & 0 & ... & H_{(Conv-DC)_1} & 0 & 0 \\ 0 & H_{(Conv-AC)_2} & 0 & ... & 0 & H_{(Conv-DC)_2} & 0 \\ 0 & 0 & H_{(Conv-AC)_k} & ... & 0 & 0 & H_{(Conv-DC)_k} \\ H_{(M-AC)_1} & 0 & 0 & ... & H_{(M-DC)_1} & 0 & 0 \\ 0 & H_{(M-AC)_2} & 0 & ... & 0 & H_{(M-DC)_2} & 0 \\ 0 & 0 & H_{(M-AC)_k} & ... & 0 & 0 & H_{(M-DC)_k} \end{bmatrix} \quad (65)$$

Where
H_{AC-AC} is the partial derivative of $hac(x)$ to θ and V_{ac}
H_{DC-AC} is the partial derivative of $hdc(x)$ to θ and $V_{ac} \leftrightarrow$ 0-matrix
H_{AC-DC} is the partial derivative of $hac(x)$ to $V_{dc} \leftrightarrow$ 0-matrix
H_{DC-DC} is the partial derivative of $hdc(x)$ to V_{dc}
$H_{Conv-AC}$ is the partial derivative of the power coupling constraint to θ and V_{ac}
$H_{Conv-DC}$ is the partial derivative of the power coupling constraint to V_{dc}
H_{M-AC} is the partial derivative of M_{factor} to θ and V_{ac}
H_{M-DC} is the partial derivative of M_{factor} to V_{dc}

The following subsection presents the partial derivatives of the additional components to the unified Jacobian matrix $H_{unified}(x)$. The AC, DC, power and voltage coupling derivative components are available in [40].

5.3 State estimation simulations

In this section, a validation of the unified WLS is provided along with a comparison with the decentralized approach. The unified WLS uses the power and voltage coupling of the converter to connect the decentralized AC and DC grids.

The unified approach of the WLS state estimator was implemented in the Julia optimization programming language [41]. It was structured in a flexible way that allows easy switching between the different test cases and scenarios (Decentralized, converter power/voltage coupling and unified). The WLS algorithm was implemented in recursion loops with dictionaries and data structures for better memory optimization and arithmetical processing. The true measurements of the hybrid VSC-HVDC/AC systems were obtained by the power-flow solver from PowerModelsACDC.jl (Julia library) [36]. The noisy measurements are calculated by adding Gaussian noise to the true measurements based on Equation (66).

$$z_{noisy} = z_{true} + N(\mu, \sigma^2) \tag{66}$$

The Gaussian noise $N(\mu, \sigma^2)$ is generated with μ equals to the true measurement and σ is calculated from Equation (67) [42]. Further details on the equation derivation are available in [31].

$$\sigma = \frac{\mu \ \%error}{100 \ \phi^{-1}\left(\frac{1+\alpha}{2}\right)} \tag{67}$$

Where α is assumed to cover 99.73% of the Gaussian distribution curve ($\phi^{-1}\left(\frac{1+\alpha}{2}\right) = 3 \ Sigma$), and $\%error$ is the additional error percentage. In this work, all noisy measurements were corrupted with 3% percentage error, except M_{factor} measurements with 1%.

The simulation study compares between the different state estimation scenarios as follow:

1. Decentralized: the systems are assumed to be separated with no data/ measurements exchange (no coupling). The Jacobian matrix is reduced to contain only AC and DC components, and multi-thread WLSs are run for each AC and DC system.

2. Converter P-Coupling: a single WLS is run centralized with the converter power coupling constraints added to the Jacobian matrix.

3. Converter PV-Coupling (unified): the power constraints and voltage coupling measurements are taken into the centralized WLS estimation, forming the unified estimation approach.

The WLS algorithm is configured to have a maximum number of iteration equal to 20 and the tolerance stop condition, related to the change of correction ($\Delta\hat{x}$), equal to 10^{-8}. The weights of the measurements are shown in Table 7.

Table 7: Measurements weights (variances R_{ii})

Measurement type	**Weight**
voltages/angles, power coupling and zero injections constraints	$1e^{-6}$
power flow and M_{factor}	$1e^{-5}$
+/- power injections	$1e^{-4}$

A hybrid VSC-HVDC/AC network was modeled to test the algorithm (5.1.1). The network is assumed to have bipolar DC links (hence $p = 2$). The following subsection presents the WLS simulation results for three scenarios: Decentralized AC and DC systems, AC/DC power coupling and unified.

5.3.1 Four(4)-AC/four(4)-DC/four(4)-AC network

The first network is comprised of two 4-bus AC systems, numbered from 1 to 4 and 5 to 8, respectively, connected by a DC grid, as shown in Figure 29. The AC systems have two AC generators at bus 1 and 6; both considered slack buses (references). The AC load is presented only at bus 8. The DC grid has 4 buses, with bus 1 as a slack bus. Bus 3 has a virtual converter is used to force the power flow direction.

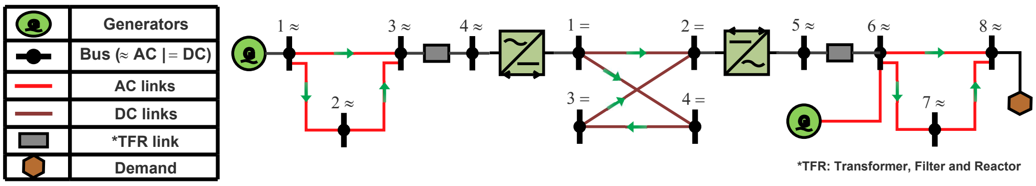

Figure 29: 4AC-4DC-4AC network.

In Table 8 and 9, the true, noisy and estimated measurements of the DC and AC systems are presented respectively, where T1 is: Decentralized, T2: with converter P-coupling, and T3: Unified. Figure 30 visualizes the accuracy performance for the three scenarios in some of the AC and DC power injection measurements. It shows the error between the true measurements against the noisy and estimated measurements. The bars represent the relative error in percentages, lower means closer to the true measurement. In Figure 30 (a), the estimation of the DC power injection at bus 3 has shown high relative error in the three estimation approaches because this measurement represents a virtual converter.

Table 8: DC systems measurements z_{DC}

Sys. #	Meas. type	True Meas.	Noisy Meas.	T1 Estimation	T2 Estimation	T3 Estimation
1	V_{dc} @ bus 1 (slack)	1.0100	1.0100	1.0100	1.0100	1.0100
	P_{inj} @ bus 1	0.111280	0.112209	0.111653	0.111236	0.111235
	P_{inj} @ bus 2	-0.111202	-0.109628	-0.111563	-0.111151	-0.11116
	P_{inj} @ bus 3	0.0001*	$9.9022e^{-5}$	$9.4749e^{-5}$	$9.6284e^{-5}$	$9.6288e^{-5}$
	P_{inj} @ bus 4	0.0	0.0	$-5.5783e^{-6}$	$-4.041e^{-6}$	$-4.038e^{-6}$

* used as a virtual converter (to route the flow).

Table 9: AC systems measurements z_{AC}

Sys. #	Meas. type	True Meas.	Noisy Meas.	T1 Estimation	T2 Estimation	T3 Estimation
1	V_{ac} @ bus 1 (slack)	1.0600	1.0600	1.0600	1.0600	1.0600
	P_{inj} @ bus 1	0.122963	0.121141	0.122597	0.122877	0.122895
	P_{inj} @ bus 4	-0.122493	-0.123621	-0.122159	-0.122443	-0.122444
	Q_{inj} @ bus 1	0.00753466	0.00756398	0.00752762	0.00754452	0.00753644
	Q_{inj} @ bus 4	0.0	0.0	$-3.5946e^{-5}$	$-1.865e^{-5}$	$-1.0725e^{-5}$
2	V_{ac} @ bus 6 (slack)	1.0600	1.0600	1.0600	1.0600	1.0600
	P_{inj} @ bus 5	0.1	0.101183	0.0997715	0.0999448	0.0999446
	P_{inj} @ bus 6	0.0505456	0.0509225	0.0495076	0.0498217	0.0498781
	P_{inj} @ bus 8	-0.15	-0.147212	-0.148724	-0.14881	-0.14882
	Q_{inj} @ bus 5	0.06	0.0614694	0.0608747	0.060879	0.0608781
	Q_{inj} @ bus 6	0.00262294	0.00261144	0.00201452	0.00201872	0.00202918
	Q_{inj} @ bus 8	-0.05	-0.0496862	-0.0504239	-0.0503197	-0.0503192

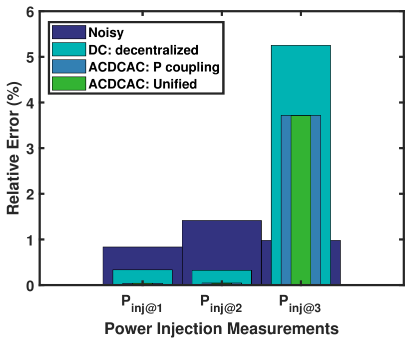

((a)) DC measurments

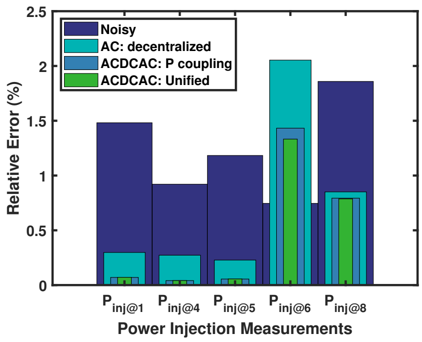

((b)) AC measurments

Figure 30: The relative error in power injection measurements

The converter power coupling measurement is presented as a power constraint equal to zero (Equation (55)), and it aims to correct the power measurements related to the converter. While the voltage coupling measurement is defined as a ratio (M_{factor}) that relates the voltage magnitudes of both sides of the converter. The unified WLS was able to accurately estimates the M_{factor} measurements and the power coupling constraints as shown in Table 10.

Table 10: The converter coupling measurements

Conv. #	Meas. type	True Meas.	Noisy Meas.	Estimated Meas.
1	Power constraint	0.0	-	$5.7070e^{-6}$
	M_{factor}	0.67685604	0.67653596	0.67674968
2	Power constraint	0.0	-	$-2.5849e^{-6}$
	M_{factor}	0.67268026	0.671752966	0.67257118

Figure 31 shows the Mean Absolute Error (MAE) of the converter measurements. In (a) the converter power coupling has minimized the error in the DC grid measurements compared to the decentralized method, it has reduced from -38.2754 dB to -46.7865 dB (14.09% less in linear form). This case concludes that on the DC side a dramatic improvement can be achieved whenever the noisy measurements are close to the converter. In (b) it shows a slightly similar impact on the AC side, the MAE has decreased by -0.6857 dB.

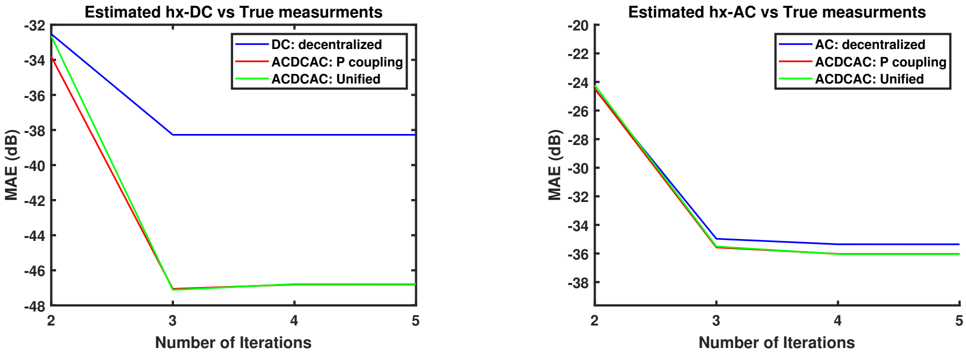

((a)) DC measurments ((b)) AC measurments

Figure 31: MAE of the AC and DC measurements in the 4AC-4DC-4AC network

The DC system states estimation are shown in Table 11. For the three different scenarios, the estimations are almost identical, and the error is lower than 5 digits ($1e^{-5}$). That is due to the low number of the DC buses and the linear feature of the DC components.

Table 11: DC systems SE: Decentralized/Power coupling/Unified

Bus #	V_{True}	V_{Est}	V_{Err}
1.0	1.0100	1.0100	0.0000
2.0	1.0084	1.0084	-0.0000
3.0	1.0087	1.0087	-0.0000
4.0	1.0094	1.0094	-0.0000

The AC side voltages and phase angles (in radian) estimations are available in Table 12, 13 and 14 for the three scenarios respectively. The unified approach has shown better estimates at bus 7 and 8 compared to the other scenarios. However, the overall error is expected to be low since the AC systems do not have many buses and branches. Figure 32 shows the relative error in the phase angles for each scenario. In (a), the P-coupling and unified approaches were able to provide 5-digits accuracy in the phase angles compared to the decentralized approach. The unified approach was able to preserve the power coupling corrections on the measurements level while improving the estimates of the voltage states using the voltage coupling (e.g. Bus 7 in Table 14).

Table 12: AC systems SE: Decentralized

Sys. #	**Bus #**	V_{True}	V_{Est}	V_{Err}	θ_{True}	θ_{Est}	θ_{Err}
1	1.0	1.0600	1.0600	-0.0000	0.0000	0.0000	0.0000
	2.0	1.0569	1.0569	-0.0000	-0.0278	-0.0277	0.0001
	3.0	1.0551	1.0551	-0.0000	-0.0601	-0.0599	0.0002
	4.0	1.0540	1.0540	-0.0000	-0.0612	-0.0610	0.0002
2	5.0	1.0615	1.0615	0.0000	0.0004	0.0003	0.0001
	6.0	1.0600	1.0600	0.0000	0.0000	-0.0000	0.0000
	7.0	1.0433	1.0432	0.0001	-0.0353	-0.0350	-0.0003
	8.0	1.0289	1.0287	0.0002	-0.0721	-0.0714	-0.0007

Table 13: AC systems SE: with converter power coupling

Sys. #	**Bus #**	V_{True}	V_{Est}	V_{Err}	θ_{True}	θ_{Est}	θ_{Err}
1	1.0	1.0600	1.0600	-0.0000	0.0000	0.0000	0.0000
	2.0	1.0569	1.0569	0.0000	-0.0278	-0.0278	-0.0000
	3.0	1.0551	1.0551	0.0000	-0.0601	-0.0601	-0.0000
	4.0	1.0540	1.0540	0.0000	-0.0612	-0.0612	-0.0000
2	5.0	1.0615	1.0615	0.0000	0.0004	0.0004	0.0000
	6.0	1.0600	1.0600	0.0000	0.0000	-0.0000	0.0000
	7.0	1.0433	1.0432	0.0001	-0.0353	-0.0351	-0.0002
	8.0	1.0289	1.0287	0.0002	-0.0721	-0.0715	-0.0006

Table 14: AC systems SE: Unified

Sys. #	**Bus #**	V_{True}	V_{Est}	V_{Err}	θ_{True}	θ_{Est}	θ_{Err}
1	1.0	1.0600	1.0600	-0.0000	0.0000	0.0000	0.0000
	2.0	1.0569	1.0569	0.0000	-0.0278	-0.0278	-0.0000
	3.0	1.0551	1.0551	0.0000	-0.0601	-0.0601	-0.0000
	4.0	1.0540	1.0540	0.0000	-0.0612	-0.0612	-0.0000
2	5.0	1.0615	1.0615	0.0000	0.0004	0.0004	0.0000
	6.0	1.0600	1.0600	0.0000	0.0000	-0.0000	0.0000
	7.0	1.0433	1.0433	0.0000	-0.0353	-0.0351	-0.0002
	8.0	1.0289	1.0287	0.0002	-0.0721	-0.0715	-0.0006

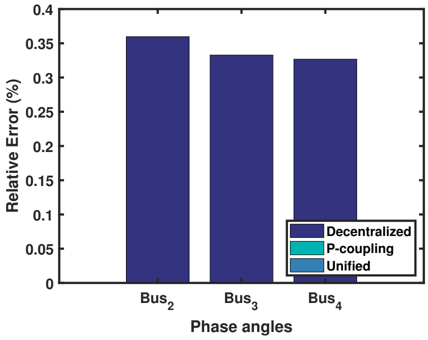

((a)) AC system #1

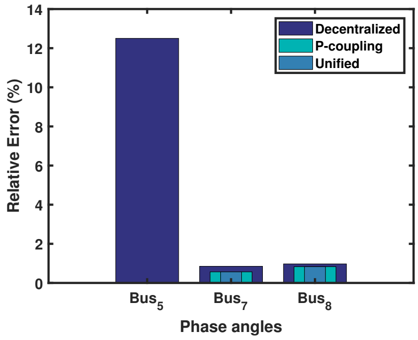

((b)) AC system #2

Figure 32: Relative error of the phase angles states in AC systems 1 and 2

6 Conclusions

In this report, a toolbox to model step-by-step the SiC MOSFET half-bridge power modules has been presented. The proposed toolbox and modelling approach significantly reduce time and efforts of converter designers to develop their own models for switching-loss analysis and converter design. Subcircuits and equations of SiC modules were firstly introduced to accurately model the drain-to-source current, antiparallel diode, parasitic capacitance and temperature dependency. Then, a step-by-step parameter extraction approach based on datasheet was proposed, which can be easily used to model other SiC MOSFET half-bridge power modules. As an example, a SPICE model was built based on the proposed modelling approach for a commercial power module. A good agreement on switching on/off waveforms is achieved between simulation and experiment results, which verifies the accuracy of the proposed modelling approach.

A toolbox to design the voltage controller of DC transformers is presented. A PI controller is used to control the output voltage of a DAB-based DC transformer. The parameters of the PI controller are designed based on the transfer function and frequency response of the DC transformer. The toolbox and modelling of the DC transformer are validated by simulation results.

Furthermore, SCADA and EMS structure and components are described and illustrated with figures. A list of the major functions and toolboxes of the modern SCADA is presented and briefly explained. An additional chapter focuses on a state estimation toolbox for hybrid VSC-HVDC/AC networks in a unified/centralized method. The toolbox was validated in a 4AC-4DC-4AC network test case, and the simulation results focusing on accuracy and performance are provided.

References

[1] Fei Wang, Edward A Jones, and Zheyu Zhang. *Characterization of wide bandgap power semiconductor devices*. Institution of Engineering & Technology, 2018.

[2] H. Sakairi, T. Yanagi, H. Otake, N. Kuroda, and H. Tanigawa. Measurement methodology for accurate modeling of SiC MOSFET switching behavior over wide voltage and current ranges. *IEEE Trans. Power Electron.*, 33(9):7314–7325, Sep. 2018.

[3] S. Yin, P. Tu, P. Wang, K. J. Tseng, C. Qi, X. Hu, M. Zagrodnik, and R. Simanjorang. An accurate subcircuit model of SiC half-bridge module for switching-loss optimization. *IEEE Trans. Ind. Appl.*, 53(4):3840–3848, July 2017.

[4] H. A. Mantooth, K. Peng, E. Santi, and J. L. Hudgins. Modeling of wide bandgap power semiconductor devices − Part I. *IEEE Trans. Electron Devices*, 62(2):423–433, 2015.

[5] K. Sun, H. Wu, J. Lu, Y. Xing, and L. Huang. Improved modeling of medium voltage SiC MOSFET within wide temperature range. *IEEE Trans. Power Electron.*, 29(5):2229–2237, 2014.

[6] Z. Duan, T. Fan, X. Wen, and D. Zhang. Improved SiC power MOSFET model considering nonlinear junction capacitances. *IEEE Trans. Power Electron.*, 33(3):2509–2517, 2018.

[7] H. Li, X. Zhao, K. Sun, Z. Zhao, G. Cao, and T. Q. Zheng. A non-segmented PSpice model of SiC MOSFET with temperature-dependent parameters. *IEEE Trans. Power Electron.*, 34(5):4603–4612, 2019.

[8] *CAS120M12BM2 − 1200 V 120 A SiC MOSFET power module.*

[9] Cadence Design System, Portland, OR, USA. *Pspice A/D Reference Guide, Version 16.5*, 2011.

[10] *Wolfspeed, LTspice and PLECS Models.*

[11] M. Noborio, Y. Kanzaki, Jun Suda, and T. Kimoto. Experimental and theoretical investigations on short-channel effects in 4H-SiC MOSFETs. *IEEE Trans. Electron Devices*, 52(9):1954–1962, 2005.

[12] *CGD15HB62P1 − Gate driver board for 1200 V SiC MOSFET power modules.*

[13] *PathWave Advanced Design System.*

[14] A. Rodríguez, A. Vázquez, D. G. Lamar, M. M. Hernando, and J. Sebastián. Different purpose design strategies and techniques to improve the performance of a dual active bridge with phase-shift control. In *2014 IEEE 15th Workshop on Control and Modeling for Power Electronics (COMPEL)*, pages 1–10, 2014.

[15] Tai-Hoon Kim. Securing communication of scada components in smart grid environment. In *International Journal of Systems Applications, Engineering & Development*, volume 5, 2011.

[16] Allen J Wood and Bruce F Wollenberg. *Power generation, operation, and control.* 01 2012.

[17] Rajib Baran Roy. Controlling of electrical power system network by using scada. In *International Journal of Scientific & Engineering Research*, volume 3, 2012.

[18] E. . Chan and H. Ebenhoh. The implementation and evolution of a scada system for a large distribution network. *IEEE Transactions on Power Systems*, 7(1):320–326, Feb 1992.

[19] Rosario Miceli. Energy management and smart grids. *Energies*, 6(4):2262–2290, 2013.

[20] D. Roberson, H. C. Kim, B. Chen, C. Page, R. Nuqui, A. Valdes, R. Macwan, and B. K. Johnson. Improving grid resilience using high-voltage dc: Strengthening the security of power system stability. *IEEE Power and Energy Magazine*, 17(3):38–47, 2019.

[21] Stuart A. Boyer. *Scada: Supervisory Control And Data Acquisition.* International Society of Automation, USA, 4th edition, 2009.

[22] Johannes Wynand Lambrechts and Saurabh Sinha. Microsensing networks for sustainable cities. 2016.

[23] D. J. Marihart. Communications technology guidelines for ems/scada systems. *IEEE Transactions on Power Delivery*, 16(2):181–188, April 2001.

[24] Jerry D. Gibson, editor. *The Communications Handbook.* CRC Press, 2 edition, 2002.

[25] J Northcote-Green and R Wilson. *Control and automation of electrical power distribution systems.* 01 2017.

[26] Practical industrial data communications. In Deon Reynders, Steve Mackay, Edwin Wright, and Steve Mackay, editors, *Practical Industrial Data Communications*, pages xi – xii. Butterworth-Heinemann, Oxford, 2004.

[27] Ashish Koushik and Rashmi Bs. 4th generation scada implementation for automation. 5:629, 04 2016.

[28] A. Sajid, H. Abbas, and K. Saleem. Cloud-assisted iot-based scada systems security: A review of the state of the art and future challenges. *IEEE Access*, 4:1375–1384, 2016.

[29] Ieee standard for scada and automation systems. *IEEE Std C37.1-2007 (Revision of IEEE Std C37.1-1994)*, pages 1–143, May 2008.

[30] Javier Herrera, Matias Mingarro, Santiago Barba, David Dolezilek, Fernando Calero, Amandeep Kalra, and Brian Waldron. New deterministic, high-speed, wide-area analog synchronized data acquisition - creating opportunities for previously unachievable control strategies. In *Power and Energy Automation Conference*, 2016.

[31] Ravindra Singh. *State Estimation in Power Distribution Network Operation.* PhD thesis, Imperial College London, 2009.

[32] M. B. D. C. Filho, A. M. L. Silva, and D. M. Falcao. Bibliography on power system state estimation (1968-1989). *IEEE Transactions on Power Systems*, 5:950–961, August 1990.

[33] A. Monticelli. *State Estimation in Electric Power Systems: A Generalized Approach.* January 1999.

[34] A. Abur and Antonio Gomez-Exposito. *Power System State Estimation: Theory and Implementation*, volume 24. Marcel Dekker, January 2004.

[35] Enrique Acha, Pedro Roncero-Sánchez, Antonio de la Villa-Jaen, Luis Castro, and Behzad Kazemtabrizi. *VSC-FACTS-HVDC: Analysis, Modelling and Simulation in Power Grids.* 04 2019.

[36] H. Ergun, J. Dave, D. Van Hertem, and F. Geth. Optimal power flow for ac/dc grids: Formulation, convex relaxation, linear approximation, and implementation. *IEEE Transactions on Power Systems*, 34(4):2980–2990, July 2019.

[37] Jun Liang, Oriol Bellmunt, and Dirk Van Hertem. *HVDC grid layouts: For Offshore and Supergrid of the Future*, pages 171–191. 03 2016.

[38] J. Zhao, A. Gomez-Exposito, M. Netto, L. Mili, A. Abur, V. Terzija, I. Kamwa, B. C. Pal, A. K. Singh, J. Qi, Z. Huang, and A. P. S. Meliopoulos. Power system dynamic state estimation: Motivations, definitions, methodologies and future work. *IEEE Transactions on Power Systems*, pages 1–1, 2019.

[39] A. Mouco and A. Abur. A robust state estimator for power systems with hvdc components. In *2017 North American Power Symposium (NAPS)*, pages 1–5, 2017.

[40] Motaz Ayiad;Helder Leite ;Hugo Martins. State estimation for hybrid vsc based hvdc/ac transmission networks. UnderReview: Energies, 2020.

[41] Jeff Bezanson, Alan Edelman, Stefan Karpinski, and Viral B Shah. Julia: A fresh approach to numerical computing. *SIAM review*, 59(1):65–98, 2017.

[42] R. Singh, B. C. Pal, and R. A. Jabr. Statistical representation of distribution system loads using gaussian mixture model. *IEEE Transactions on Power Systems*, 25(1):29–37, 2010.

[43] A. Endruschat, C. Novak, H. Gerstner, T. Heckel, C. Joffe, and M. Marz. A universal SPICE field-effect transistor model applied on SiC and GaN transistors. *IEEE Trans. Power Electron.*, 34(9):9131–9145, Sep. 2019.